



## Technical note: Evaluation of profile retrievals of aerosols and trace gases for MAX-DOAS measurements under different aerosol scenarios based on radiative transfer simulations

Xin Tian <sup>1,2</sup>, Yang Wang <sup>\*3#</sup>, Steffen Beirle <sup>3</sup>, Pinhua Xie <sup>\*2,4,5,6</sup>, Thomas Wagner <sup>3</sup>, Jin

5 Xu <sup>2</sup>, Ang Li <sup>2</sup>, Steffen Dörner <sup>3</sup>, Bo Ren <sup>2,6</sup>, Xiaomei Li <sup>2</sup>

1. Information Materials and Intelligent Sensing Laboratory of Anhui Province, Institutes of Physical Science and Information Technology, Anhui University, Hefei, 230601, China;

2. Key laboratory of Environmental Optical and Technology, Anhui Institute of optics and Fine Mechanics, Chinese Academy of Science, Hefei, 230031, China;

10 3. Max Planck Institute for Chemistry, Mainz, 55128, Germany;

# now at EUMETSAT, Darmstadt. Germany;

4. CAS Center for Excellence in Urban Atmospheric Environment, Institute of Urban Environment, Chinese Academy of Sciences, Xiamen, 361021, China;

5. University of Chinese Academy of Sciences, Beijing, 100049, China;

15 6. School of Environmental Science and Optoelectronic Technology, University of Science and Technology of China, Hefei, 230026, China;

*Author:* Xin Tian (xtian@ahu.edu.cn)

*Correspondence to:* Pinhua Xie (phxie@aiofm.ac.cn); Yang Wang (y.wang@mpic.de)

20 **Abstract:** Ground-based Multi-AXis Differential Optical Absorption Spectroscopy (MAX-DOAS) is a state of the art remote sensing technique for deriving vertical profiles of trace gases and aerosols. However, MAX-DOAS profile inversions under aerosol pollution scenarios are challenging because of the complex radiative transfer and limited information content of the measurements. In this study, the performances

25 of two inversion algorithms were evaluated for various aerosol pollution scenarios based on synthetic slant column densities (SCDs) derived from radiative transfer simulations. One inversion algorithm is based on optimal estimation, the other uses a parameterized approach. In this analysis, 3 types of profile shapes for aerosols and NO<sub>2</sub> were considered: exponential, Boltzmann, and Gaussian. First, the systematic



deviations of the retrieved aerosol profiles from the input profiles were investigated. For most cases, the AODs of the retrieved profiles were found to be systematically lower than the input values, and the deviations increased with increasing AOD. Especially for the optimal estimation algorithm and for high AOD, these findings might explain part of the deviations between the AOD retrieved from MAX-DOAS and sun photometers in previous studies. For the optimal estimation algorithm the agreement with the input values can be improved by optimizing the covariance matrix of the *a priori* uncertainties. Second, the aerosol effects on the NO<sub>2</sub> profile retrieval were tested. Here, especially for the optimal estimation algorithm, a systematic dependence on the NO<sub>2</sub> VCD was found with a strong relative overestimation of the retrieved results for low NO<sub>2</sub> VCDs and an underestimation for high NO<sub>2</sub> VCDs. In contrast, the dependence on the aerosol profiles was found to be rather low. In general, both inversion schemes can well retrieve the near-surface values of aerosol extinction and trace gases concentrations.

15

## 1 Introduction

In recent years, several large-scale aerosol pollution incidents in China (Hu et al., 2014; Huang et al., 2014; Wang et al., 2014; Zhang et al., 2015) have drawn increasing attention due to their effects on atmospheric visibility and health. Atmospheric aerosols also exert direct and indirect effects on global climate change and radiative balance (Seinfeld and Pandis, 1998; IPCC, 2007). The physical and chemical properties, and the spatial-temporal distributions of aerosols can both affect remote sensing

20



measurements of trace gases in the atmosphere (Seinfeld and Pandis, 1998; Quinn and Coffmann, 1998; Bond et al., 2001; Sheridan et al., 2001). Measuring the optical properties of aerosols, understanding the role of aerosols in atmospheric processes, and assessing the effects of aerosols on remote sensing observations of trace gases are

5 important goals in the study of atmospheric pollution.

The ground-based Multi-AXis Differential Optical Absorption Spectroscopy (MAX-DOAS) technique can be performed with a relatively simple set-up and very low power consumption in the ultraviolet (UV) and visible (Vis) spectral range to synchronously measure the vertical distributions of aerosol optical extinction and concentrations of

10 several trace gases (e.g., NO<sub>2</sub>, SO<sub>2</sub>, HCHO, HONO, and CHOCHO) in the troposphere (Hönninger and Platt, 2002; Hönninger et al., 2004; Wittrock et al., 2004; Wagner et al., 2004; Frieß et al., 2006). Spectra of scattered-sunlight are measured at different elevation angles (EAs) by the MAX-DOAS instrument. The spectra are analyzed by the DOAS technique (Platt and Stutz, 2008), which makes use of the characteristic

15 “fingerprint” absorptions of the different trace gases with respect to a reference spectrum taken for zenith. The results of the spectral fitting process are the so-called differential slant column densities (DSCDs) of the trace gases and the oxygen collision complex (O<sub>2</sub>-O<sub>2</sub> or O<sub>4</sub>), with the DSCD defined as the difference between the trace-gas concentration integrated along the effective light path and the corresponding integrated

20 trace-gas concentration in the zenith sky reference spectrum. The MAX-DOAS technique basically utilizes the EA dependence of differential absorption structures of O<sub>4</sub> to derive the aerosol optical depth (AOD) and the vertical distribution of the aerosol



extinction. The vertical profiles and vertical column densities (VCDs) of trace gases can be retrieved from the EA dependence of DSCDs using also the result of the aerosol profile inversion from MAX-DOAS (Irie et al., 2008, 2009; Li et al., 2010; Clémer et al., 2010; Hartl and Wenig, 2013; Hendrick et al., 2014; Vlemmix et al., 2015; Frieß et al., 2006).

Recent research on MAX-DOAS has focused on the following aspects: (1) profile inversion algorithms (Hönninger and Platt, 2002; Wagner et al., 2004; Frieß et al., 2006, 2011; Clémer et al., 2010; Hay, 2010; Vlemmix et al., 2011; Yilmaz, 2012; Hartl and Wenig, 2013; Holla, 2013; Wang et al., 2013a, b; Zielcke, 2015; Bösch et al., 2018; Beirle et al., 2019; Friedrich et al., 2019; Spinei et al., 2019; Frieß et al., 2019); (2) long-term observation of trace gases and aerosols (e.g., Irie et al., 2008a; Roscoe et al., 2010; Li et al., 2013; Ma et al., 2013; Pinardi et al., 2013; Hendrick et al., 2014; Kanaya et al., 2014; Wang et al., 2014; Chan et al., 2015; Tian et al., 2017, 2018; Wang et al., 2017a); (3) cloud identification and data correction (Gielen et al., 2014; Wagner et al., 2014, 2016; Wang et al., 2014); and (4) satellite and model data validation (e.g., Halla et al., 2011; Ma et al., 2013; Pinardi et al., 2013; Chan et al., 2015; De Smedt et al., 2015; Vlemmix et al., 2015; Jin et al., 2016; Drosoglou et al., 2017; Wang et al., 2017b; Boersma et al., 2018; Liu et al., 2018). In this study we focus on the first aspect. At present, algorithms for the retrieval of vertical profiles from MAX-DOAS measurements can be separated into optimal estimation methods (OEMs) (Rodgers, 2000) and parameterized algorithms, which describe the shapes of atmospheric profiles with a limited set (usually 2 to 3) of parameters. In Frieß et al. (2019), different MAX-



DOAS inversion schemes have been compared for synthetic input data for AODs up to 1 (plus a fog and two cloud scenarios). Given the importance and complexity of the aerosol effects on the atmospheric radiative transfer, it is also important to study the impact of heavy aerosol loads on the MAX-DOAS inversion algorithm.

5 Here, we investigate the effects of the aerosol extinction and optical properties, including single-scattering albedo (SSA) and the asymmetry parameter (AP), on the retrieval of aerosols and trace gas profiles in the UV and Vis under low to heavy aerosol pollution scenarios based on simulated DSCDs. We compare the aerosol and trace gas profiles retrieved from MAX-DOAS by two inversion algorithms (PriAM and MAPA,  
10 for details see below) with the input values (used as input for the DSCD simulations) for different aerosol scenarios. For the trace gas retrievals, we apply 2 retrieval strategies where either the retrieved or the input aerosol profile is used.

This manuscript is organized as follows. Section 2 briefly describes the basic settings for the aerosol and NO<sub>2</sub> profile inversions and for the tests of the profile comparisons.

15 The analysis strategy of this study is presented in Section 2.1. The model scenarios and radiative transfer model (RTM) settings are specified in Section 2.2. The 2 profile retrieval algorithms (PriAM and MAPA v. 0.98) are described in Section 2.3. The effects of aerosols on the profile retrievals are discussed in Section 3.

## 20 **2 Basic settings and tests**

### **2.1 Analysis strategy**



The analysis strategy of this study is depicted in **Fig. 1**. A set of atmospheric scenarios, viewing geometries, single-scattering albedos, and asymmetry parameters was used to simulate the SCDs of traces gases and O<sub>4</sub>, which will be described in detail in Section 2.2. The first step was to quantitatively evaluate the effect of different aerosol loads on the aerosol inversion. For that purpose the simulated O<sub>4</sub> SCDs were used as input for the aerosol profile retrievals. The retrieved and input aerosol profiles were then compared in order to characterize the effect of the aerosol properties (in particular the AODs) on the retrieved aerosol profiles. The second step was to quantitatively evaluate the effect of different aerosol loads on the trace gas inversion.

10

## 2.2 RTM parameters

Before the effects of different aerosol loads on the retrieval of aerosol and trace gas profiles were analyzed, some basic parameters were prescribed for simulating the O<sub>4</sub> and trace gas SCDs for the assumed ‘true’ profiles in the RTM. In this study, the SCIAMACHY radiative transfer model (SCIATRAN) (version 2.2, Rozanov et al., 2005) is used in the forward model calculations. Here it is important to note that while SCIATRAN is also used in PriAM, in the MAPA algorithm a different RTM (MCARTIM, Deutschmann et al., 2011) is used. The differences of the simulated O<sub>4</sub> dSCDs by both models are discussed in section 3.1.2.

20 SCIATRAN models radiative transfer processes in the terrestrial atmosphere and ocean in the spectral range from the ultraviolet to the thermal infrared including all significant radiative transfer processes, e.g., the Rayleigh scattering, scattering by aerosol and



cloud particles, and absorption by gaseous components and aerosols (Rozanov et al., 2014). The RTM used in this section was SCIATRAN version 2.2. The Monte Carlo Atmospheric Radiative Transfer Inversion Model (McARTIM) is a full spherical Monte Carlo model without polarization (Deutschmann et al., 2011). In a recent  
5 intercomparison activity within the project FRM4DOAS (<https://frm4doas.aeronomie.be/>), in general very good agreement (deviations up to a few percent) between MCARTIM and SCIATRAN version 2.2 was found with the largest deviations for cases with fog or shallow box profiles (Frieß et al., 2018). It should also be noted that the agreement between MCARTIM and SCIATRAN v3.0 is better  
10 than with SCIATRAN v2.2. The differences between O<sub>4</sub> DSCDs simulated by SCIATRAN and MCARTIM are further investigated in section 3.1.2.

Retrievals based on synthetic SCDs for various viewing geometries in the UV and Vis were performed. The dependencies on the retrieval parameters and settings, different measurement viewing geometries, and different aerosol and trace gas profile shapes  
15 were identified by comparison of the results to those of the standard settings. As standard settings we chose wavelengths at 360 nm and 477 nm, elevation angles of 1°, 2°, 3°, 4°, 5°, 6°, 8°, 15°, 30°, and 90° (the same as the settings in the CINDI 2 campaign, Kreher et al., 2020). Three different profile shapes were used as a-priori, which are described by either Exponential, Gaussian, or Boltzmann functions of altitude  $z$  as  
20 follows:

Exponential:  $f_E(z) = A_E(h_E) \times \exp\left(\frac{-z}{h_E}\right)$  with scale height  $h_E$ ,



Gaussian:  $f_G(z) = A_G(h_G, \sigma) \times \exp\left(\frac{-(z-h_G)^2}{2\sigma^2}\right)$  with peak height  $h_G$ , and the

full width at half maximum (FWHM)  $\sigma$ ,

Boltzmann:  $f_B(z) = \frac{A_B(h_B)}{1 + \exp\left(\frac{-(z-h_B)}{0.3}\right)}$  with effective profile height  $h_B$ .

The normalization factors  $A_E$ ,  $A_G$ , and  $A_B$  are determined by numerical integration  
5 from 0 to 4 km altitude such that the integrals of  $f_E$ ,  $f_G$  and  $f_B$  equal 1, respectively.

For RTM calculations, vertical profiles of the aerosol extinction  $\varepsilon$  and  $\text{NO}_2$   
concentration  $c$  are generated by multiplying  $f$  with the respective a-priori column:

$$\varepsilon = f(z) \times \tau,$$

$$c = f(z) \times \text{VCD}.$$

10 Figure S1 displays the corresponding vertical profiles for the different shapes. Table 1  
lists the parameters used for RTM, including solar/viewing geometry, a-priori  
AOD/VCD, and parameters for the different profile shapes. The profile shape scenarios  
are introduced in detail in Section 3.1.

## 15 2.3 Description of the retrieval algorithms

The retrieval algorithms used in the comparison included PriAM and MAPA, which are  
listed in **Table 2**.

### 2.3.1 PriAM algorithm

20 The PriAM profile inversion algorithm of aerosol extinction and trace gas concentration  
developed by the Anhui Institute of Optics and Fine Mechanics, Chinese Academy of





Sciences (AIOFM, CAS), in cooperation with the Max Planck Institute for Chemistry (MPIC) (Wang et al., 2013a and b, 2016), is based on the nonlinear optimal estimation method using the Levenberg–Marquardt modified Gauss–Newton numerical iteration procedure (Rodgers, 2000). PriAM uses the radiative transfer model (RTM) SCIATRAN version 2.2 (Rozañov et al., 2005) to calculate the weighting functions and other simulated quantities. PriAM consists of a 2-step inversion procedure. In the first step, aerosol extinction profiles are retrieved from the dependence of the O<sub>4</sub> DSCDs on elevation angle. The single-scattering albedo and asymmetry parameters have to be prescribed for the aerosol retrieval, e.g. based on other auxiliary measurements. Subsequently, profiles of the trace gas number density are retrieved from the respective DSCDs in each MAX-DOAS elevation angle sequence (Wang et al., 2017). In order to avoid negative concentrations in the retrieved results (which are not possible in the actual atmosphere), the retrievals are performed in logarithmic space. Here it should be noted that since the distribution probabilities of the retrieved profiles around the *a priori* profiles become asymmetric due to the inversion in logarithmic space, the sensitivity of the inversion to large values is greater than the sensitivity in linear space (Wang et al., 2019). PriAM can retrieve trace gas and aerosol profiles on any arbitrary vertical grid. In this study, vertical layers with 200-m resolution in the altitude range below 4.0 km were used.

20

### 2.3.2 MAPA algorithm

The Mainz profile algorithm (MAPA) is a parameter-based inversion method using a



Monte Carlo (MC) approach developed by the Max Planck Institute for Chemistry (MPIC) (Beirle et al., 2019). Here we use MAPA v0.991, which is basically the same algorithm as described in Beirle et al., 2019 (v0.98), with only slight differences in the flagging procedure.

5 The radiative transfer model used in MAPA (McArtim, Deutschmann et al., 2011) for calculating each parameter in the lookup tables (LUTs) is a full spherical Monte Carlo model. MAPA also comprises a 2-step inversion procedure. First, the aerosol profile is retrieved based on O<sub>4</sub> DSCDs. In this step, other input parameters include the errors of the O<sub>4</sub> DSCD, the O<sub>4</sub> VCD and information about the viewing geometry (elevation  
10 angle (EA), solar zenith angle (SZA), and relative azimuth angle (RAA)). Next, the trace gas profiles are retrieved based on the aerosol profiles derived in step 1 and the trace gas DSCDs (and their errors). Three parameters (layer height, profile shape, and integrated column (AOD or VCD)) of the aerosol and trace gas profiles are derived in the inversion. The final profiles are weighted averages of the best matching profiles for  
15 the given trace gas dSCDs. The details of MAPA can be found in Beirle et al. (2019). It is worth noting that the maximum AOD in MAPA is 3, since higher AODs were not included in the RTM look-up table; therefore, only aerosol scenarios with AOD < 3 were included in this study for MAPA.

### 20 **3 Results and discussion**

In order to simulate the effects of different aerosol loads on the MAX-DOAS profile inversion algorithms, the aerosol and trace gas profiles were set up with 5 AOD and 5



VCD values as presented in **Tables 1** and different height parameters as shown in **Table 1**).

In order to limit the number of investigated profiles, first a sensitivity study with PriAM was carried for the selection of the profile shapes which best represent the variety of realistic profile shapes. Based on the result shown in **Figs. S2 to S4** it turned out that one height parameter is mostly representative for the parameterization with Gaussian and Boltzmann profiles. For the exponential profiles, two height parameters were chosen.

The settings of the 4 chosen profile shapes are listed in **Table 1**. The 4 profiles are exponential profiles with scale heights of 0.5 km and 1.0 km, respectively, Gaussian profiles with the peak height at 1.0 km and FWHM of 0.5 km, and Boltzmann profiles with a height of 1.5km.

A similar sensitivity study was also performed for the trace gas profiles. The results of the sensitivity analysis (**Figs. S5 to S7**) for NO<sub>2</sub> profiles are consistent with the findings for the aerosol profiles. Thus the settings of the NO<sub>2</sub> profile shapes for all further tasks are the same as for the aerosol profile in **Table 1**.

### 3.1 Aerosol results

The effect of different AOD on the retrieval of aerosol profiles are presented for a scenario with SZA = 60°, RAA = 120°, SSA = 0.9, and AP = 0.72. Note that similar results were found for different scenarios. In addition, the effects of SSA and AP are further explored in Section 3.1.4.



### 3.1.1 Aerosol profile comparison of PriAM and MAPA

**Fig. 2** shows the relative deviations between the input aerosol profiles and the corresponding profiles retrieved by PriAM and MAPA for the different profile shapes and AOD scenarios. Note that the comparison of the retrieved and input profiles is shown in **Fig. S8**. The absolute deviations are shown in **Fig. S9**. The results reveal that both PriAM and MAPA can overall well retrieve the 4 different profile shapes (**Figs. S8** of the supplement). Similar results were derived for the aerosol retrievals at 360 nm and 477 nm. However, also systematic differences are found, which increase as the AOD increases. The systematic deviations between the retrieved and input aerosol profiles for PriAM were smaller than for MAPA at AOD <1.0. For the exponential profiles with scale heights of 1.0 km, the systematic deviations between the retrieved and input aerosol profiles were the smallest among the 4 profile shapes. The derived profiles for exponential profiles with scale heights of 0.5 km were in better agreement for PriAM than for MAPA. The maximum absolute deviations primarily occurred at heights < 1.0 km. Here it is interesting to note that the parameterization used in MAPA does not include pure exponential profiles, but only combined profiles with a (shallow) box profile at the bottom and an exponential profile on top. This limitation can explain the large systematic deviations for MAPA retrievals especially at low altitudes. For the Boltzmann-shaped profiles, the height around which the maximum systematic deviations for PriAM and MAPA often occurred was 1.0 km, but for AOD > 1.0, the systematic deviations for PriAM in the 200-m layer were greater than for MAPA. In brief, the concentrations of the 200–400 m layer retrieved by PriAM were moderately



larger than those of the input profiles for  $AOD > 1.0$ . Thus, better agreement for the Boltzmann profiles was found for MAPA than for PriAM. For the Gaussian-shaped profiles, both PriAM and MAPA could well retrieve the lifted layer. The width of the lifted layer retrieved by MAPA was close to the truth, although the aerosol extinction was underestimated. PriAM underestimated the width of the lifted layer, but the aerosol extinction was closer to the input value (**Fig. S8** of the supplement). The height at which the maximum systematic deviations for the Gaussian-shaped profiles mainly occurred was 1.5 km. The relative deviations between the retrieved and input aerosol profiles for different AOD scenarios are similar for the same retrieval algorithm with the relative deviations for  $AOD > 1.0$  obviously greater than for  $AOD < 1.0$ . But the relative deviation does not increase with the increase in AOD.

### 3.1.2 Differences of the $O_4$ SCDs simulated by SCIATRAN and MCARTIM

PriAM and MAPA use different RT models, which might partly explain systematic differences. In order to quantify the impact of the differences between SCIATRAN and MCARTIM,  $O_4$  DSCDS calculated by MCARTIM are compared to those calculated by SCIATRAN for selected cases.

Because the aerosol properties used in the MAPA LUT ( $SSA = 0.95$  and  $AP = 0.68$ ) are different from those used for the simulations of the  $O_4$  dSCDs by SCIATRAN ( $SSA = 0.90$  and  $AP = 0.72$ ), two sets of  $O_4$  DSCDs for SSA and AP ( $SSA = 0.90$  or  $0.95$  and  $AP = 0.72$  or  $0.68$ ) were simulated by MCARTIM.

The comparison results for the  $O_4$  DSCDs (**Fig. S10**) show that systematic differences between the SCIATRAN and MCARTIM simulations using the same SSA and AP of



0.9 and 0.72, respectively, are up to 9%. If also different aerosol properties were used, these differences increased further.

In the next step, the differences of the retrieval results for the different input DSCDs are investigated. The corresponding results are shown in **Fig. S11**. Interestingly, it is  
5 found that the exact choice of the aerosol optical properties has only a small influence on the results.

Using McArtim for the calculation of synthetic dSCDs, i.e. consistent RTM in forward model and inversion, results in much better agreement, in particular for low AOD. Thus, the large relative deviations for MAPA seen in **Fig. 7** are partly explained by the  
10 differences in RTM. For the Gaussian profiles, the larger differences at high AODs occur due to the obvious overestimation of the width of the lifted layer.

### 3.1.3 Sensitivity study of the *a priori* profile and the *a priori* profile covariance matrix

15 In order to improve the profile inversion accuracy for high AODs, the influence of the *a priori* profile and the *a priori* profile covariance matrix ( $S_a$ ) was examined for PriAM. Here it should be noted that an exponential shape with an AOD of 0.2 was used as universal *a priori* profile in this study. The influence of the *a priori* profile on the retrieved aerosol profile was analyzed by changing the *a priori* profile to different  
20 aerosol profile shapes. Also, in addition to an AOD of 0.2 a second AOD value of 2.0 is used. The *a priori* profiles used in the sensitivity test are presented in **Fig. 3**. Here it should be noted that either the exponential profile shapes (universal *a priori* profile in



PriAM in this study) or the same profile shapes (Boltzmann or Gaussian) as the input profiles are also used as *a priori* profiles (referred to as ‘corresponding a priori profiles’ in the following). The relative deviations of retrieved profiles using the different *a priori* profiles with the input profiles are shown in **Fig. 4**. It is found that the inversion results of the aerosol profile were slightly improved by changing the *a priori* profiles to the corresponding profile shapes, and that for the high AOD scenarios the inversion results were further improved by increasing the AOD of the corresponding *a priori* profile (**Fig. S12**). However, increasing the AOD of the universal (exponential) *a priori* profile exhibited no effect on the inversion results. It is worth noting that when the input aerosol extinction coefficient was small, the use of *a priori* profiles with high AOD often yielded unrealistic results.

The  $S_a$  is the covariance matrix of the *a priori* profile ( $N \times N$ ), and its diagonal elements are the square of the *a priori* state uncertainties. The universal *a priori* settings of  $S_a$  in this study was such that the diagonal elements decreased exponentially with height. As a consequence, the smaller the  $S_a$  values, the more the inversion results depends on the prior state vector. The diagonal elements of  $S_a$  for the standard settings of the aerosol profile were set as the square of 10% of the *a priori* profile. The effect of different  $S_a$  values on the retrieval of the 4 aerosol profiles was studied, and the results for an AOD of 5.0 are shown in **Fig. 5** (The profile results show that the systematic deviations between the retrieved and input profile increase with the increase of the AOD, so a high AOD of 5.0 was selected to show the impact for an extreme case). The 4 diagonal elements of  $S_a$  were set to the squares of 6%, 10%, 20%, and 50% of the *a priori* profile.



For the exponential profiles with a scale height of 0.5 km, the correlation between the retrieved and input aerosol profiles decreased with increasing  $S_a$ . The correlation could be improved by increasing the  $S_a$  values for the Gaussian and Boltzmann aerosol profile shapes. In particular, the retrieved surface extinctions and scale heights could be improved by increasing the  $S_a$ . This is primarily due to the fact that the higher the  $S_a$  values, the lower the upper limits are for the inversion. When the  $S_a$  values were too large, however, the retrieved aerosol profiles in the upper layer were more unstable. The highest correlation coefficient was found when the diagonal elements of  $S_a$  were set to the square of 20% of the a priori profile for the Boltzmann profile with an AOD of 5.0. For the Gaussian profile, the correlation coefficient was highest with the diagonal elements of  $S_a$  in 50% of the a priori profile.

#### 3.1.4 Comparison of retrieved and input $O_4$ DSCD for PriAM and MAPA

The modeled  $O_4$  DSCDs corresponding to the aerosol profiles retrieved by PriAM and MAPA were compared to the input  $O_4$  DSCDs simulated by the RTM. The comparison results are shown in **Fig. 6** for the different aerosol profile shapes and the 5 AOD values for 360 and 477 nm. Note that only the results for  $AOD < 3.0$  were derived from MAPA. Also the slopes, intercepts, and correlation coefficients are shown in **Fig. 6**. The correlation coefficients ( $r^2$  values) were  $> 0.99$  for both the PriAM and MAPA results. Also the slopes are very close to unity. Therefore, it can be concluded that the discrepancies of the retrieved aerosol profiles from the input profiles were not caused by failed convergences of the retrievals but must be related to systematic performances





of the inversion algorithms in solving the ill-conditioned problem.

### 3.1.5 AOD comparison of PriAM and MAPA

**Fig. 7** shows the deviations of the AODs retrieved by PriAM and MAPA with the input  
5 AODs for the 4 selected aerosol profiles and 5 AOD values. Both PriAM and MAPA  
underestimate in general the input AODs. For the exponential aerosol profiles with a  
scale height of 0.5 km, the relative deviations of the retrieved AODs by PriAM and  
MAPA compared to the input AODs are less than 20% for most AODs. . In contrast,  
much worse agreement is found for the exponential profiles with scale height of 1.0 km.  
10 The deviations between the retrieved and input profiles are  $> 20\%$  and are similar for  
PriAM and MAPA. The main reason is that the retrieved scale height for exponential  
profile of 1.0km by PriAM and MAPA is significantly lower than the input profile.  
Especially for low AOD the AODs retrieved by PriAM are closer to the input AODs  
than those retrieved by MAPA. Part of the systematic underestimation of the MAPA  
15 AODs for exponential profiles is probably caused by the differences of the RTM  
(SCIATRAN v2.2) and settings (SSA=0.9, AP=0.72) used for the simulation of the  
input O<sub>4</sub> dSCDs and for the MAPA algorithm (MCARTIM, SSA=0.95, AP=0.68), see  
**Fig. S11**. Another reason might be, as mentioned in section 3.1.2, the limitation to  
accurately describe purely exponential profile shapes.  
20 For the Boltzmann and Gaussian profile shapes the relative deviations between the  
retrieved and the input AODs increased with increasing AODs for both PriAM and  
MAPA. The largest deviations are  $>50\%$  for large AODs.



### 3.1.6 Effect of single scattering albedo and asymmetry parameter used in the inversion of the retrieved aerosol profiles

The effects of single-scattering albedo (SSA) and asymmetry parameter (AP) used in the forward model of the aerosol profile inversion by PriAM were examined. First, a single aerosol profile was used to simulate the O<sub>4</sub> DSCDs for different SSA and AP values. Next, the simulated O<sub>4</sub> DSCDs were used to retrieve the aerosol extinction profiles by PriAM using the same SSA and AP values. The retrieved aerosol profiles for all SSA and AP values are shown in **Fig. S14**. These results reveal that especially for low AODs the retrieved aerosol extinction profiles are very consistent for these scenarios. The relative and systematic deviations of the resulting aerosol extinction profiles to the input profiles are presented in **Fig. 8 and Fig. S15**. The results are consistent with those presented in **Figs. 2 and S9**. It is worth noting that the relative deviation for the Boltzmann aerosol profiles retrieved for SSA = 0.9 and AP = 0.72 was smaller than for the other scenarios. In the next step, the effect of incorrect SSA and AP values (**Table 3**) on the aerosol profile inversion was studied using the PriAM standard settings with SSA = 0.9 and AP = 0.72 for the simulation of the O<sub>4</sub> DSCDs. The systematic deviations of the retrieved profiles from the profiles with the correct SSA and AP values are presented in **Fig. 9**. It was found that when the SSA was smaller than the input value, the retrieved extinction profiles were larger than the input profiles and vice versa. It is worth noting that the result at 0 km is found to be opposite. For the AP the opposite dependency was found. The effect of incorrect SSA and AP values on the aerosol profiles retrieved by PriAM increased with increasing AOD with deviations



increasing from 0.01 to 1.5 as the AOD increased from 0.1 to 5.0.

### 3.2 NO<sub>2</sub> results

First, the effects of different aerosol extinction profiles on the trace gas profile inversion  
5 for 5 NO<sub>2</sub> VCDs were examined using aerosol profiles with 4 AODs (0.3, 1.0, 3.0, and  
5.0) (AOD = 5.0 was not included for MAPA). Two strategies (S1 and S2) were  
employed to retrieve the NO<sub>2</sub> profiles (see **Section 2.1**). Here, as for the aerosol  
inversions, also the scenario with SZA = 60°, RAA = 120°, SSA = 0.9, and AP = 0.72  
was used. For the NO<sub>2</sub> profiles, the exponential profile shape with a VCD of  $1.0 \times 10^{16}$   
10 molecules cm<sup>-2</sup> was utilized as the universal *a priori* profile for PriAM.

#### 3.2.1 Comparison of NO<sub>2</sub> profiles retrieved by PriAM and MAPA

**Fig. 10 and Fig. S19** shows the relative and systematic deviations of 4 typical NO<sub>2</sub>  
profiles retrieved by PriAM and MAPA using S1 with the input NO<sub>2</sub> profiles for the  
15 Boltzmann aerosol profile shapes with 3 AODs (0.13, 1.0, and 3.0) and 5 VCD values.  
The results reveal that the systematic deviations between the NO<sub>2</sub> profiles retrieved by  
both PriAM and MAPA and the input NO<sub>2</sub> profiles are similar and relatively small,  
despite the differences in level of agreement of the aerosol inversion. For the same  
aerosol conditions, the systematic deviations between the retrieved NO<sub>2</sub> profiles and  
20 the input values increase with increasing NO<sub>2</sub> VCDs, although the relative deviations  
stay constant (**Fig. S10**). It is worth noting that the relative deviations between the  
retrieved NO<sub>2</sub> profiles and the input values for low NO<sub>2</sub> VCDs were significantly higher



than for high NO<sub>2</sub> VCDs for an AOD of 3.0. The systematic deviations between the retrieved NO<sub>2</sub> profiles and the input NO<sub>2</sub> profile for the exponential NO<sub>2</sub> profiles with scale height of 0.5 km were mainly found below 1.0 km. The systematic deviations between the retrieved NO<sub>2</sub> profile and the input NO<sub>2</sub> profile appeared below 2.0 km for

5 the other three profile shapes, with the maximum deviations occurring at 1.0 km and 0.2 km. The reason for this finding is that the sensitivity above 1.0 km gradually decreases with increasing AOD, making it impossible to correctly retrieve the NO<sub>2</sub> values at high altitudes. The artificial smoothing effect of the profile inversion algorithm mistakenly overestimates the NO<sub>2</sub> concentrations around 500 m to

10 compensate for the underestimation of the NO<sub>2</sub> concentrations above 1.0 km. In other words, the profile inversion algorithm yields another solution for the ill-conditioned problem in order to achieve convergence between the retrieved and measured SCDs under the control of the *a priori* profile and its uncertainty covariance.

In the real atmosphere, the profiles of aerosols and NO<sub>2</sub> are often quite different.

15 Therefore, the effect of 4 typical aerosol profile shapes on the retrieval of Boltzmann NO<sub>2</sub> profiles by PriAM and MAPA using S1 with 3 AODs (0.3, 1.0, and 3.0) and 5 VCD values was further studied. The results showed that the relative and absolute deviations (**Figs.11** and **Fig.S21**) between the Boltzmann NO<sub>2</sub> profiles retrieved for the 4 aerosol profile shapes and the input NO<sub>2</sub> profiles was basically the same, which means

20 that the influence of the aerosol profile shapes on the retrieval of the NO<sub>2</sub> profiles is small. The NO<sub>2</sub> profiles for the 5 VCDs retrieved for scenarios S1 and S2 by PriAM were further compared with the input NO<sub>2</sub> profiles for the 4 AOD conditions (0.3, 1.0,



3.0, and 5.0) (**Fig. 12**). The systematic deviations between the retrieved NO<sub>2</sub> profiles using S1 and the input values were smaller than those for scenario S2, mainly because the retrieved scale heights for the S1 inversions were closer to the input scale height (**Fig. S22** of the supplement). An interesting phenomenon was the occurrence of some singular values in the upper layers of the retrieved profiles for low NO<sub>2</sub> VCDs (mainly for NO<sub>2</sub> VCD <  $1 \times 10^{16}$  molecules cm<sup>-2</sup>). The NO<sub>2</sub> profiles retrieved for scenario S1 were more stable than the profiles for scenario S2, with fewer singular values. When the AOD was large but the NO<sub>2</sub> VCD was small, the systematic deviations of the NO<sub>2</sub> number density at high altitudes was rather large, mainly because the lack of upper-level information for the NO<sub>2</sub> profiles made the inversion results more dependent on the *a priori* profile. When the VCD increased, although the box-AMF at high altitudes was small, the NO<sub>2</sub> number density at high altitudes also contribute to the SCDs due to the high NO<sub>2</sub> VCD. Thus, when the AOD was large, the value at high altitudes of the NO<sub>2</sub> profile can be better retrieved for increased NO<sub>2</sub> VCDs.

15 The smaller the covariance matrix of the *a priori* profile (*S<sub>a</sub>*), the more the retrieved profile depends on the *a priori* profile, which determines the degree to which the retrieved profile deviates from the *a priori* profile. As standard value of the diagonal elements for retrieval of NO<sub>2</sub> profiles, we used the square of 50% of the *a priori* profile. And an *a priori* profile of exponential shape is used for NO<sub>2</sub> retrieval (shown in **Fig.**

20 **13**), which may cause the great difference between the retrieved and input NO<sub>2</sub> profile, especially for the Gaussian and Boltzmann NO<sub>2</sub> profiles. In order to reduce the occurrence of single outliers in the upper layer of the NO<sub>2</sub> profile, the *S<sub>a</sub>* was reduced,



thus making the retrieved profile more dependent on the *a priori* profile. The effect of the Sa reduction on the retrieval of the 4 NO<sub>2</sub> profile types was examined for AODs of 0.3 and 5.0 (**Fig. 14**). The Sa reduction increased the stability of the NO<sub>2</sub> profile retrievals for low NO<sub>2</sub> VCDs while simultaneously increasing the retrieved scale height.

5 The increase of Sa for high AOD conditions did not improve the inversion results but instead increased the occurrence of single outliers. For low NO<sub>2</sub> VCDs, the overestimation of the NO<sub>2</sub> profile above 2.0 km can be explained by the higher values of the *a priori* profile at the upper layers, because when the AOD is large, the information content for the NO<sub>2</sub> distribution at upper layers is very sparse, and the

10 inversion results mainly depend on the *a priori* profile.

### **3.2.2 Comparison of the retrieved NO<sub>2</sub> DSCD by PriAM and MAPA and the input NO<sub>2</sub> DSCD for scenario (S1)**

The NO<sub>2</sub> DSCDs retrieved by PriAM and MAPA for scenario S1 were compared with

15 the input NO<sub>2</sub> DSCDs for 4 AOD scenarios and 5 VCDs, as shown in **Fig. 15**. The correlations between the NO<sub>2</sub> DSCDs retrieved by PriAM and the input values were similar, and for both algorithms values very close to 1.0 were found. Also for the slopes values close to 1.0 were found.

### **20 3.2.3 Comparison of the NO<sub>2</sub> VCDs retrieved by PriAM and MAPA**

The NO<sub>2</sub> VCDs retrieved by PriAM and MAPA were compared with the input NO<sub>2</sub> VCDs for 3 AOD scenarios and 5 VCDs, as shown in **Fig. 16**. The NO<sub>2</sub> VCDs were



retrieved for PriAM for scenarios S1 and S2, and for MAPA for scenario S1. The VCDs  
retrieved by MAPA were closer to the input VCDs than those retrieved by PriAM. The  
retrievals of NO<sub>2</sub> VCDs by MAPA and PriAM were only slightly affected by the AOD.  
However, especially for PriAM, a strong and systematic dependence of the relative  
5 deviations on the NO<sub>2</sub> VCD was found for all profile shapes. While for small NO<sub>2</sub>  
VCDs the retrieved VCDs systematically overestimate the true NO<sub>2</sub> VCDs (by up to  
60% for PriAM), for large NO<sub>2</sub> VCDs a systematic underestimation is observed (up to  
-20%). For Gaussian and Boltzmann profiles the deviations are larger than for the  
exponential profiles. Best agreement is found for NO<sub>2</sub> VCDs around  $1 \times 10^{16}$  molec.  
10 /cm<sup>2</sup>. Here it should, however, be noted that while for low NO<sub>2</sub> VCDs the relative  
deviations are large, the absolute deviations are rather small.

#### 4 Conclusions

Given that severe air pollution often occurs during autumn and winter in China, the  
15 effects of different aerosol conditions on the accuracy of MAX-DOAS profile retrieval  
were studied. The effects of aerosols on MAX-DOAS retrievals of aerosols and NO<sub>2</sub>  
profiles were examined by assuming a series of aerosol scenarios with 3 aerosol profile  
shapes (exponential, Boltzmann, and Gaussian) with AODs/VCDs ranging from 0.1 to  
5.0. In addition, a series of NO<sub>2</sub> scenarios was assumed with the same profile shapes  
20 and various VCD values.

In a first step, the effects of the assumed single-scattering albedo (SSA) and asymmetric  
parameter (AP) on the aerosol profile inversion was investigated. It was found that the



retrieved aerosol extinction profiles are very consistent if the same SSA and AP values are used for the simulations of the O<sub>4</sub> DSCDs and the PriAM inversions. If incorrect SSA and AP values were used, the retrieved extinction coefficients were smaller than the input values in the case of too low of AP or too high SSA assumed in the profile inversion and vice versa (with opposite behavior for the surface values).

Next, the systematic deviations of the PriAM and MAPA profile retrievals from the input profiles for different aerosol conditions were examined. We found that both algorithms can reasonably retrieve the 4 aerosol profile shapes, especially for AODs < 1.0, but for most cases the retrieved values systematically underestimate the true AODs. The smallest deviations (typically <20%) were found for exponential profile shapes, with a scale height of 0.5 km. Large deviations (up to >50%) are found for the other profile shapes, especially for high AODs. This is an important finding and can probably explain deviations of retrieved AODs from MAX-DOAS and sun photometers in several previous studies (e.g. Tirpitz et al., 2021). In general, the relative deviations of the MAPA results depend less on the AOD than the PriAM results. For MAPA, part of the differences between input and retrieved AODs can be explained by the differences in RTM model. It should also be noted that for the Gaussian profiles, both PriAM and MAPA could retrieve the lifted layer. However, PriAM underestimated the width of the lifted layer and the extinction coefficient at the peak, while MAPA overestimated the width of the lifted layer and significantly underestimated the aerosol extinctions at the peak.





Then, for PriAM, the effect of using different *a priori* profiles and *a priori* profile covariance matrices ( $S_a$ ) was studied. The results showed that the retrieval results of the aerosol profiles were slightly improved when the same *a priori* profile shape as the input profile shape was used. In addition, the inversion results were more consistent

5 with the input profiles when the AOD of the *a priori* profile was increased for high AOD scenarios. The effect of the  $S_a$  value for the 4 aerosol shapes was investigated for the extreme scenario with an AOD of 5.0. It was found that the correlation could be improved by increasing the  $S_a$  values for all aerosol profile shapes, mainly because of improved values of the retrieved surface extinction and scale height.

10 Also the modeled  $O_4$  DSCDs corresponding to the aerosol profiles retrieved by PriAM and MAPA were compared to  $O_4$  DSCDs simulated by the RTM for the input aerosol profiles. The averaged correlation coefficients of the modeled and simulated  $O_4$  DSCDs were  $> 0.99$  for both PriAM and MAPA, indicating that a possible non-convergence of the profile retrievals is not a reason for the systematic discrepancies of retrieved profiles

15 from the input profiles.

In the next part, the effects of the aerosol retrieval on the  $NO_2$  profile retrieval were studied for PriAM and MAPA. Two strategies were utilized to retrieve the  $NO_2$  profiles, in which either the retrieved or the input aerosol profiles served as input for the retrievals of the  $NO_2$  profiles in strategy 1 (S1) and strategy 2 (S2), respectively.

20 Strategy S1 was applied both to PriAM and MAPA, while strategy S2 was only applied to PriAM. From these studies several conclusions could be drawn: The relative deviations of the retrieved  $NO_2$  VCDs do only slightly depend on the AOD or the shape



of the aerosol profiles. In contrast, especially for PriAM, a systematic dependence on the NO<sub>2</sub> VCD was found. For low NO<sub>2</sub> VCDs the retrieved NO<sub>2</sub> VCDs largely underestimate the true NO<sub>2</sub> VCDs by up to 60%, while for high NO<sub>2</sub> VCDs a systematic underestimation up to -20% is found. Here it should be noted that in spite of the large  
5 relative deviations for low NO<sub>2</sub> VCDs, the absolute deviations are rather small.

The increase of the Sa values did not improve the inversion results for high AODs, but instead lead to the occurrence of single outliers.

#### Author contributions

10 XT, YW, SB, PX and TW contributed to design the research. SB performed the MAPA profile inversions and calculated the input profiles. SD convert O<sub>4</sub> data format to MAPA input data format. BR and XL processed the SCIATRAN data. XT performed the data analyses and wrote the manuscript. JX and AL supervised this study and provided suggestions for the manuscript. PX and YW revised this manuscript. TW and SB  
15 developed the manuscript.

#### Acknowledgment

This study was supported by the National Natural Science Foundation of China (Grant Nos.: 41530644, U19A2044, 41975037), Natural Science Foundation of Anhui  
20 Province (Grant Nos.: 2008085QD183, 2008085QD182), and the Open Fund of Key Laboratory of Environmental Optics and Technology, Chinese Academy of Sciences (Grant Nos.: 2005DP173065-2019-04).



## References

- Beirle, S., Dörner, S., Donner, S., Remmers, J., Wang, Y., Wagner, T.: The Mainz profile algorithm (MAPA). *Atmos. Meas. Tech.*, 12, 1785–1806, 2019
- 5 Bobrowski, N., Hönniger, G., Galle, B., Platt, U.: Detection of bromine monoxide in a volcanic plume, *Nature*, 423, 273–276, 2003.
- Boersma, K. F., Eskes, H.J., Richter, A., De Smedt, I., Lorente, A., Beirle, S., van Geffen, J.H. G. M., Zara, M., Peters, E., Van Roozendaal, M., Wagner, T., Maasakkers, J.D., van der A, R.J.,  
10 Nightingale, J., De Rudder, A., Irie, H., Pinardi, G., Lambert, J.-C., Compernelle, S.C.: Improving algorithms and uncertainty estimates for satellite NO<sub>2</sub> retrievals: results from the quality assurance for the essential climate variables (QA4ECV) project. *Atmos. Meas. Tech.*, 11, 6651–6678, 2018.
- Bond, D.W., Zhang, R., Tie, X., Brasseur, G., Huffman, G., Orville, R.E., Boccippio, D.J., NO<sub>x</sub>  
15 production by lightning over the continental United States. *J. Geophys. Res.-Atmos.* 106 (D21), 27701–27710, 2001.
- Bösch, T., Rozanov, V., Richter, A., Peters, E., Rozanov, A., Wittrock, F., Merlaud, A., Lampel, J., Schmitt, S., de Haij, M., Berkhout, S., Henzing, B., Apituley, A., den Hoed, M., Vonk, J.,  
20 Tiefengraber, M., Müller, M., and Burrows, J. P.: BOREAS – a new MAX-DOAS profile retrieval algorithm for aerosols and trace gases, *Atmos. Meas. Tech.*, 11, 6833–6859, <https://doi.org/10.5194/amt-11-6833-2018>, 2018.
- 25 Chan, K.L., Hartl, A., Lam, Y.F., Xie, P.H., Liu, W.Q., Cheung, H.M., Lampel, J., Pohler, D., Li, A., Xu, J., Zhou, H.J., Ning, Z., Wenig, M.O.: Observations of tropospheric NO<sub>2</sub> using ground based MAX-DOAS and OMI measurements during the Shanghai World Expo 2010, *Atmos. Environ.*, 119, 41–58, 2015.
- 30 Clémer, K., Van Roozendaal, M., Fayt, C., Hendrick, F., Hermans, C., Pinardi, G., Spurr, R., Wang, P., and De Mazière, M.: Multiple wavelength retrieval of tropospheric aerosol optical properties from MAXDOAS measurements in Beijing, *Atmos. Meas. Tech.*, 3, 863–878, <https://doi.org/10.5194/amt-3-863-2010>, 2010.
- 35 de Haan, J. F., Bosma, P. B., and Hovenier, J. W.: The adding method for multiple scattering calculations of polarized light, *Astron. Astrophys.*, 183, 371–391, 1987.
- De Smedt, I., Stavrakou, T., Hendrick, F., Danckaert, T., Vlemmix, T., Pinardi, G., Theys, N., Lerot, C., Gielen, C., Vigouroux, C., Hermans, C., Fayt, C., Veefkind, P., Müller, J.-F., and Van  
40 Roozendaal, M.: Diurnal, seasonal and long-term variations of global formaldehyde columns inferred from combined OMI and GOME-2 observations, *Atmos. Chem. Phys.*, 15, 12519–12545, <https://doi.org/10.5194/acp-15-12519-2015>, 2015.



- Deutschmann, T., Beirle, S., Frieß, U., Grzegorski, M., Kern, C., Kritten, L., Platt, U., Prados-Romañ, C., Pukite, J., Wagner, T., Bodo, W., Pfeilsticker, K.: The Monte Carlo atmospheric radiative transfer model McArtim: Introduction and validation of Jacobians and 3D features, *J. Quantitative. Spectrosc. Ra.*, 112, 1119–1137, 2011.
- 5 Drosoglou, T., Bais, A.F., Zyrichidou, I., Kouremeti, N., Poupkou, A., Liora, N., Giannaros, C., Koukouli, M. E., Balis, D., Melas, D.: Comparisons of ground-based tropospheric NO<sub>2</sub> MAX-DOAS measurements to satellite observations with the aid of an air quality model over the Thessaloniki area, Greece, *Atmos. Chem. Phys.*, 17, 5829–5849, 2017.
- 10 Feingold, G., W. R. Cotton, S. M. Kreidenweis, Davis, J. T.: Impact of giant cloud condensation nuclei on drizzle formation in marine stratocumulus: Implications for cloud radiative properties, *J. Atmos. Sci.*, 56, 4100–4117, 1999.
- 15 Friedrich, M. M., Rivera, C., Stremme, W., Ojeda, Z., Arellano, J., Bezanilla, A., García-Reynoso, J. A., and Grutter, M.: NO<sub>2</sub> vertical profiles and column densities from MAX-DOAS measurements in Mexico City, *Atmos. Meas. Tech.*, 12(4), 2545–2565, 2019.
- 20 Frieß, U., Beirle, S., Bösch, T., Friedrich, M.M., Hendrick, F., PETERS, A., Richter, A., van Roozendael, M., Spinei, E., Tirpitz, J.-L., Vlemmix, T., Wagner, T.: Comparison of algorithms for the retrieval of aerosol and trace gas vertical profiles using synthetic MAX-DOAS Data, Results from the FRM4DOAS Project, presentation at the 2nd CINDI-2 Workshop, Mutters (Austria), 14–15 March 2018 ([https://frm4doas.aeronomie.be/ProjectDir/2nd-CINDI2-WS/Friess\\_-\\_FRM4DOAS\\_Round\\_Robin.pdf](https://frm4doas.aeronomie.be/ProjectDir/2nd-CINDI2-WS/Friess_-_FRM4DOAS_Round_Robin.pdf)), 2018.
- 25 Frieß, U., Beirle, S., Alvarado Bonilla, L., Bösch, T., Friedrich, M. M., Hendrick, F., PETERS, A., Richter, A., van Roozendael, M., Rozanov, V. V., Spinei, E., Tirpitz, J.-L., Vlemmix, T., Wagner, T., Wang, Y.: Intercomparison of MAX-DOAS vertical profile retrieval algorithms: studies using synthetic data, *Atmos. Meas. Tech.*, 12, 2155–2181, <https://doi.org/10.5194/amt-12-2155-2019>, 2019.
- 30 Frieß, U., Monks, P. S., Remedios, J. J., Rozanov, A., Sinreich, R., Wagner, T., and Platt, U.: MAX-DOAS O<sub>4</sub> measurements: A new technique to derive information on atmospheric aerosols: 2. Modeling studies, *J. Geophys. Res.*, 111, D14203, doi:10.1029/2005JD006618, 2006.
- 35 Frieß, U., Sihler, H., Sander, R., Pöhler, D., Yilmaz, S., and Platt, U.: The vertical distribution of BrO and aerosols in the Arctic: Measurements by active and passive differential optical absorption spectroscopy, *J. Geophys. Res.*, 116, D00R04, <https://doi.org/10.1029/2011JD015938>, 2011.
- 40 Gielen, C., Van Roozendael, M., Hendrick, F., Pinardi, G., Vlemmix, T., De Bock, V., De Backer, H., Fayt, C., Hermans, C., Gillotay, D., and Wang, P.: A simple and versatile cloud screening method for MAX-DOAS retrievals, *Atmos. Meas. Tech.*, 7, 3509–3527, doi:10.5194/amt-7-3509-2014, 2014.



- 5 Halla, J. D., Wagner, T., Beirle, S., Brook, J. R., Hayden, K. L., O'Brien, J. M., Ng, A., Majonis, D.,  
Wenig, M. O., McLaren, R.: Determination of tropospheric vertical columns of NO<sub>2</sub> and aerosol  
optical properties in a rural setting using MAX-DOAS, *Atmos. Chem. Phys.*, 11, 12475–12498,  
2011.
- 10 Hartl, A. and Wenig, M. O.: Regularisation model study for the least-squares retrieval of aerosol  
extinction time series from UV/Vis MAX-DOAS observations for a ground layer profile  
parameterisation, *Atmos. Meas. Tech.*, 6, 1959–1980, doi:10.5194/amt-6-1959-2013, 2013.
- Hay, T.: MAX-DOAS measurements of bromine explosion events in McMurdo Sound, Antarctica,  
PhD thesis, University of Canterbury, 2010.
- 15 Hendrick, F., Müller, J.-F., Clémer, K., Wang, P., De Mazière, M., Fayt, C., Gielen, C., Hermans,  
C., Ma, J. Z., Pinardi, G., Stavrakou, T., Vlemmix, T., and Van Roozendaal, M.: Four years of  
ground-based MAX-DOAS observations of HONO and NO<sub>2</sub> in the Beijing area, *Atmos. Chem.  
Phys.*, 14, 765–781, https://doi.org/10.5194/acp-14-765-2014, 2014.
- 20 Holla, R.: Reactive Halogen Species above Salt Lakes and Salt Pans, PhD thesis, University of  
Heidelberg, 2013.
- Hönninger, G., and Platt, U.: The role of BrO and its vertical distribution during surface ozone  
depletion at Alert, *Atmos. Environ.*, 36, 2481–2489, 2002.
- 25 Hönninger, G., von Friedeburg, C., and Platt, U.: Multi axis differential optical absorption  
spectroscopy (MAX-DOAS), *Atmos. Chem. Phys.*, 4, 231–254, doi:10.5194/acp-4-231-2004, 2004.
- 30 Hu, J.L., Wang, Y.G., Ying, Q., Zhang, H.L.: Spatial and temporal variability of PM<sub>2.5</sub> and PM<sub>10</sub>  
over the North China Plain and the Yangtze River Delta, China[J]. *Atmos. Environ.*, 95, 598-609,  
2014.
- 35 Huang, R.J., Zhang, Y.L., Bozzetti, C., Ho, K.F., Cao, J.J., Han, Y.M., Daellenbach, K.R., Slowik,  
J.G., Platt, S.M., Canonaco, F., Zotter, P., Wolf, R., Pieber, S.M., Bruns, E.A., Crippa, M., Ciarelli,  
G., Piazzalunga, A., Schwikowski, M., Abbazade, G., Schnelle-Kreis, J., Zimmermann, R., An,  
Z.S., Szidat, S., Baltensperger, U., El Haddad, I., Prevot, A.S.H.: High secondary aerosol  
contribution to particulate pollution during haze events in China[J]. *Nature*, 514, 218-222, 2014.
- 40 IPCC, 2007. *Climate change 2007: the physical science basis. Contribution of Working Group I to  
the Fourth Assessment Report of the Intergovernmental Panel on Climate Change.* Cambridge  
University Press, Cambridge, UK and New York, NY, USA.
- Irie, H., Kanaya, Y., Akimoto, H., Iwabuchi, H., Shimizu, A., and Aoki, K.: First retrieval of  
tropospheric aerosol profiles using MAX-DOAS and comparison with lidar and sky radiometer  
measurements, *Atmos. Chem. Phys.*, 8, 341–350, doi:10.5194/acp-8-341-2008, 2008a.



- Irie, H., Kanaya, Y., Akimoto, H., Tanimoto, H., Wang, Z., Gleason, J. F., and Bucsela, E. J.: Validation of OMI tropospheric NO<sub>2</sub> column data using MAX-DOAS measurements deep inside the North China Plain in June 2006: Mount Tai Experiment 2006, *Atmos. Chem. Phys.*, 8, 6577–6586, doi:10.5194/acp-8-6577-2008, 2008b.
- Jin, J.L., Ma, J.Z., Lin, W.L., Zhao, H.R., Shaiganfar, R., Beirle, S., Wagner, T.: MAX-DOAS measurements and satellite validation of tropospheric NO<sub>2</sub> and SO<sub>2</sub> vertical column densities at a rural site of North China, *Atmos. Environ.*, 133, 12-25, 2016.
- Kanaya, Y., Irie, H., Takashima, H., Iwabuchi, H., Akimoto, H., Sudo, K., Gu, M., Chong, J., Kim, Y. J., Lee, H., Li, A., Si, F., Xu, J., Xie, P.-H., Liu, W.-Q., Dzhola, A., Postylyakov, O., Ivanov, V., Grechko, E., Terpugova, S., and Panchenko, M.: Long-term MAX-DOAS network observations of NO<sub>2</sub> in Russia and Asia (MADRAS) during the period 2007–2012: instrumentation, elucidation of climatology, and comparisons with OMI satellite observations and global model simulations, *Atmos. Chem. Phys.*, 14, 7909–7927, <https://doi.org/10.5194/acp-14-7909-2014>, 2014.
- Kreher, K., Van Roozendaal, M., Hendrick, F., Apituley, A., Dimitropoulou, E., Frieß, U., Richter, A., Wagner, T., Abuhassan, N., Ang, L., Anguas, M., Bais, A., Benavent, N., Bösch, T., Bognar, K., Borovski, A., Bruchkouski, I., Cede, A., Chan, K. L., Donner, S., Drosoglou, T., Fayt, C., Finkenzeller, H., Garcia-Nieto, D., Gielen, C., Gómez-Martín, L., Hao, N., Herman, J. R., Hermans, C., Hoque, S., Irie, H., Jin, J., Johnston, P., Khayyam Butt, J., Khokhar, F., Koenig, T. K., Kuhn, J., Kumar, V., Lampel, J., Liu, C., Ma, J., Merlaud, A., Mishra, A. K., Müller, M., Navarro-Comas, M., Ostendorf, M., Pazmino, A., Peters, E., Pinardi, G., Pinharanda, M., PETERS, A., Platt, U., Postylyakov, O., Prados-Roman, C., Puentedura, O., Querel, R., Saiz-Lopez, A., Schönhardt, A., Schreier, S. F., Seyler, A., Sinha, V., Spinei, E., Strong, K., Tack, F., Tian, X., Tiefengraber, M., Tzirpitz, J.-L., van Gent, J., Volkamer, R., Vrekoussis, M., Wang, S., Wang, Z., Wenig, M., Wittrock, F., Xie, P. H., Xu, J., Yela, M., Zhang, C., and Zhao, X.: Intercomparison of NO<sub>2</sub>, O<sub>4</sub>, O<sub>3</sub> and HCHO slant column measurements by MAX-DOAS and zenith-sky UV-Visible spectrometers during the CINDI-2 campaign, *Atmos. Meas. Tech.*, 13, 2169-2208, 2020.
- Li, X., Brauers, T., Shao, M., Garland, R. M., Wagner, T., Deutschmann, T., and Wahner, A.: MAX-DOAS measurements in southern China: retrieval of aerosol extinctions and validation using ground-based in-situ data, *Atmos. Chem. Phys.*, 10, 2079–2089, doi:10.5194/acp-10-2079-2010, 2010.
- Li, X., Brauers, T., Hofzumahaus, A., Lu, K., Li, Y. P., Shao, M., Wagner, T., and Wahner, A.: MAX-DOAS measurements of NO<sub>2</sub>, HCHO and CHOCHO at a rural site in Southern China, *Atmos. Chem. Phys.*, 13, 2133–2151, <https://doi.org/10.5194/acp-13-2133-2013>, 2013.
- Liu, F., van der A, R. J., Eskes, H., Ding, J.Y., Mijling, B.: Evaluation of modeling NO<sub>2</sub> concentrations driven by satellite-derived and bottom-up emission inventories using in situ measurements over China, *Atmos. Chem. Phys.*, 18, 4171–4186, 2018.



- 5 Ma, J. Z., Beirle, S., Jin, J. L., Shaiganfar, R., Yan, P., and Wagner, T.: Tropospheric NO<sub>2</sub> vertical column densities over Beijing: results of the first three years of ground-based MAXDOAS measurements (2008–2011) and satellite validation, *Atmos. Chem. Phys.*, 13, 1547–1567, <https://doi.org/10.5194/acp-13-1547-2013>, 2013.
- 10 Pinardi, G., Van Roozendael, M., Abuhassan, N., Adams, C., Cede, A., Clémer, K., Fayt, C., Frieb, U., Gil, M., Herman, J., Hermans, C., Hendrick, F., Irie, H., Merlaud, A., Navarro Comas, M., Peters, E., PETERS, A. J. M., Puentedura, O., Richter, A., Schönhardt, A., Shaiganfar, R., Spinei, E., Strong, K., Takashima, H., Vrekoussis, M., Wagner, T., Wittrock, F., and Yilmaz, S.: MAXDOAS formaldehyde slant column measurements during CINDI: intercomparison and analysis improvement, *Atmos. Meas. Tech.*, 6, 167–185, 2013.
- 15 Platt, U., and Stutz, J.: *Differential optical absorption spectroscopy principles and applications*, Springer, 2008.
- Rodgers, C. D.: *Inverse Methods for Atmospheric Sounding: Theory and Practice*, Ser. Atmos. Oceanic Planet. Phys., World Scientific Publishing, 2000.
- 20 Roozendael, M. V., Post, P., Hermans, C., Lambert, J. C., and Fayt, C.: Retrieval of BrO and NO<sub>2</sub> from UV-visible observations, *Sounding the Troposphere from Space*, Springer, Berlin, Heidelberg, 155–165, 2003.
- 25 Roscoe, H. K., Van Roozendael, M., Fayt, C., du Piesanie, A., Abuhassan, N., Adams, C., Akrami, M., Cede, A., Chong, J., Clémer, K., Friess, U., Gil Ojeda, M., Goutail, F., Graves, R., Griesfeller, A., Grossmann, K., Hemerijckx, G., Hendrick, F., Herman, J., Hermans, C., Irie, H., Johnston, P. V., Kanaya, Y., Kreher, K., Leigh, R., Merlaud, A., Mount, G. H., Navarro, M., Oetjen, H., Pazmino, A., Perez-Camacho, M., Peters, E., Pinardi, G., Puentedura, O., Richter, A., Schönhardt, A., Shaiganfar, R., Spinei, E., Strong, K., Takashima, H., Vlemmix, T., Vrekoussis, M., Wagner, T.,  
30 Wittrock, F., Yela, M., Yilmaz, S., Boersma, F., Hains, J., Kroon, M., PETERS, A., and Kim, Y. J.: Intercomparison of slant column measurements of NO<sub>2</sub> and O<sub>4</sub> by MAXDOAS and zenith-sky UV and visible spectrometers, *Atmos. Meas. Tech.*, 3, 1629–1646, 2010.
- 35 Rozanov, A., Rozanov, V., Burrows, J.P., A numerical radiative transfer model for aspherical planetary atmosphere: combined differential–integral approach involving the Picard iterative approximation. *J. Quant. Spectrosc. Radiat. Transfer*, 69(4), 491–512, 2001.
- 40 Rozanov, A., Rozanov, V., Buchwitz, M., Kokhanovsky, A., Burrows, J.P.: SCIATRAN 2.0 - A new radiative transfer model for geophysical applications in the 175–2400 nm spectral region, in: *Atmospheric Remote Sensing: Earth's Surface, Troposphere, Stratosphere and Mesosphere – I*, *Advances in Space Research*, 39, 1015–1019, 2005.
- Rozanov, V.V., Dinter, T., Rozanov, A.V., Wolanin, A., Bracher, A., Burrows, J.P.: Radiative transfer modeling through terrestrial atmosphere and ocean accounting for inelastic processes: Software



- package SCIATRAN. *J. Quant. Spectrosc. Radiat. Transfer*, 194, 65-85, 2017.
- Rozanov, V.V., Kokhanovsky, A. A.: The solution of the vector radiative transfer equation using the discrete ordinates technique: selected applications. *Atmos. Res.*, 79, 241–265, 2006.
- 5 Rozanov, V.V., Rozanov, A.V., Kokhanovsky, A.A., Burrows, J.P.: Radiative transfer through terrestrial atmosphere and ocean: Software package SCIATRAN, *J. Quant. Spectrosc. Radiat. Transfer*, 133, 13-71, 2014.
- 10 Seinfeld, J. H. and Pandis, S. N.: Atmospheric chemistry and physics: From air pollution to climate change, 2nd Edn., John Wiley and Sons, Hoboken, NJ, 2006.
- Sheridan, P.J., Delene, D.J., Ogren, J.A.: Four years of continuous surface aerosol measurements from the Department of Energy's Atmospheric Radiation Program Southern Great Plains Cloud and Radiation Testbed site, *J. Geophys. Res.*, 106, 20735–20747, 2001.
- 15 Spinei et al.: Fast aerosol extinction coefficient profile estimation from MAXDOAS UV/VIS measurements, in preparation, 2019.
- 20 Spurr, R.: LIDORT and VLIDORT: Linearized pseudo-spherical scalar and vector discrete ordinate radiative transfer models for use in remote sensing retrieval problems, in: *Light Scattering Reviews 3*, edited by: Kokhanovsky, A., Springer Praxis Books, Springer Berlin Heidelberg, 229–275, [https://doi.org/10.1007/978-3-540-48546-9\\_7](https://doi.org/10.1007/978-3-540-48546-9_7), 2008.
- 25 Stammes, P., de Haan, J. F., and Hovenier, J.W.: The polarized internal radiation field of a planetary atmosphere, *Astron. Astrophys.*, 225, 239–259, 1989.
- Tian, X., Xie, P.H., Xu, J., Li, A., Wang, Y., Qin, M., Hu, Z.K.: Long-term observations of tropospheric NO<sub>2</sub>, SO<sub>2</sub> and HCHO by MAX-DOAS in Yangtze River Delta area, China. *Journal of Environmental Sciences*, 71, 207-221, 2018.
- 30 Tian, X., Xie, P.H., Xu, J., Wang, Y., Li, A., Wu, F.C., Hu, Z.K., Liu, C., Zhang, Q.: Ground-based MAX-DOAS observations of tropospheric formaldehyde VCDs and comparisons with the CAMS model at a rural site near Beijing during APEC 2014. *Atmos. Chem. Phys.*, 19, 3375–3393, 2019
- 35 Tirpitz, J.-L., Frieß, U., Hendrick, F., Alberti, C., Allaart, M., Apituley, A., Bais, A., Beirle, S., Berkhout, S., Bognar, K., Bösch, T., Bruchkouski, I., Cede, A., Chan, K. L., den Hoed, M., Donner, S., Drosoglou, T., Fayt, C., Friedrich, M. M., Frumau, A., Gast, L., Gielen, C., Gomez-Martín, L., Hao, N., Hensen, A., Henzing, B., Hermans, C., Jin, J., Kreher, K., Kuhn, J., Lampel, J., Li, A., Liu, C., Liu, H., Ma, J., Merlaud, A., Peters, E., Pinardi, G., Piters, A., Platt, U., Puentedura, O., Richter, A., Schmitt, S., Spinei, E., Stein Zweers, D., Strong, K., Swart, D., Tack, F., Tiefengraber, M., van der Hoff, R., van Roozendael, M., Vlemmix, T., Vonk, J., Wagner, T., Wang, Y., Wang, Z., Wenig, M., Wiegner, M., Wittrock, F., Xie, P., Xing, C., Xu, J., Yela, M., Zhang, C., and Zhao, X.: Intercomparison of MAX-DOAS vertical profile retrieval algorithms: studies on field data from the





- CINDI-2 campaign, *Atmos. Meas. Tech.*, 14, 1–35, <https://doi.org/10.5194/amt-14-1-2021>, 2021.
- Vlemmix, T., Peters, A. J. M., Berkhout, A. J. C., Gast, L. F. L., Wang, P., and Levelt, P. F.: Ability of the MAX-DOAS method to derive profile information for NO<sub>2</sub>: can the boundary layer and free troposphere be separated?, *Atmos. Meas. Tech.*, 4, 2659–2684, <https://doi.org/10.5194/amt-4-2659-2011>, 2011.
- Vlemmix, T., Hendrick, F., Pinardi, G., De Smedt, I., Fayt, C., Hermans, C., Peters, A., Wang, P., Levelt, P., and Van Roozendaal, M.: MAX-DOAS observations of aerosols, formaldehyde and nitrogen dioxide in the Beijing area: comparison of two profile retrieval approaches, *Atmos. Chem. Phys.*, 8, 941–963, [doi:10.5194/amt-8-941-2015](https://doi.org/10.5194/amt-8-941-2015), 2015.
- Wagner, T., Apituley, A., Beirle, S., Dörner, S., Friess, U., Remmers, J., and Shaiganfar, R.: Cloud detection and classification based on MAX-DOAS observations, *Atmos. Meas. Tech.*, 7, 1289–1320, [doi:10.5194/amt-7-1289-2014](https://doi.org/10.5194/amt-7-1289-2014), 2014.
- Wagner, T., Beirle, S., Brauers, T., Deutschmann, T., Frieß, U., Hak, C., Halla, J. D., Heue, K. P., Junkermann, W., Li, X., Platt, U., and Pundt-Gruber, I.: Inversion of tropospheric profiles of aerosol extinction and HCHO and NO<sub>2</sub> mixing ratios from MAX-DOAS observations in Milano during the summer of 2003 and comparison with independent data sets, *Atmos. Meas. Tech.*, 4, 2685–2715, <https://doi.org/10.5194/amt-4-2685-2011>, 2011.
- Wagner, T., Beirle, S., Remmers, J., Shaiganfar, R., Wang, Y.: Absolute calibration of the colour index and O<sub>4</sub> absorption derived from Multi AXis (MAX-)DOAS measurements and their application to a standardised cloud classification algorithm, *Atmos. Meas. Tech.*, 9, 4803–4823, 2016.
- Wagner, T., Burrows, J. P., Deutschmann, T., Dix, B., von Friedeburg, C., Frieß, U., Hendrick, F., Heue, K.-P., Irie, H., Iwabuchi, H., Kanaya, Y., Keller, J., McLinden, C. A., Oetjen, H., Palazzi, E., Petritoli, A., Platt, U., Postlyakov, O., Pukite, J., Richter, A., van Roozendaal, M., Rozanov, A., Rozanov, V., Sinreich, R., Sanghavi, S., and Wittrock, F.: Comparison of box-airmass-factors and radiances for Multiple-Axis Differential Optical Absorption Spectroscopy (MAX-DOAS) geometries calculated from different UV/visible radiative transfer models, *Atmos. Chem. Phys.*, 7, 1809–1833, <https://doi.org/10.5194/acp-7-1809-2007>, 2007.
- Wagner, T., Dix, B., von Friedeburg, C., Friess, U., Sanghavi, S., Sinreich, R., and Platt, U.: MAX-DOAS O<sub>4</sub> measurements: A new technique to derive information on atmospheric aerosols—Principles and information content, *J. Geophys. Res.*, 109, D22205, [doi:10.1029/2004JD004904](https://doi.org/10.1029/2004JD004904), 2004.
- Wagner, T., Erle, F., Marquard, L., Otten, C., Pfeilsticker, K., Senne, T., Stutz, J., and Platt, U.: Cloudy sky optical paths as derived from differential optical absorption spectroscopy observations, *J. Geophys. Res.*, 103, D19, 25 307–25 321, 1998.



- 5 Wang, T., Hendrick, F., Wang, P., Tang, G., Clémer, K., Yu, H., Fayt, C., Hermans, C., Gielen, C., Müller, J.-F., Pinardi, G., Theys, N., Brenot, H., and Van Roozendael, M.: Evaluation of tropospheric SO<sub>2</sub> retrieved from MAX-DOAS measurements in Xianghe, China, *Atmos. Chem. Phys.*, 14, 11149–11164, <https://doi.org/10.5194/acp-14-11149-2014>, 2014.
- 10 Wang, Y., Li, A., Xie, P.H., Chen, H., Xu, J., Wu, F.C., et al., Retrieving vertical profile of aerosol extinction by multi-axis differential optical absorption spectroscopy. *Acta Phys. Sin.* 62 (18), 180705-1–180705-12, 2013a.
- 15 Wang, Y., Wagner, T., Li, A., Xie, P.H., Wu, D.X., Chen, H., Mou, F.S., Zhang, J., Xu, J., Wu, F.C., Liu, W.Q., Zeng, Y.: Research of classification of cloud and aerosol using multi-axis differential optical absorption spectroscopy. *Acta Phys. Sin.* 63 (11), 110708, 2014.
- 20 Wang, Y., Beirle, S., Lampel, J., Koukouli, M., De Smedt, I., Theys, N., Li, A., Wu, D., Xie, P., Liu, C., Van Roozendael, M., Stavrou, T., Müller, J.-F., and Wagner, T.: Validation of OMI, GOME-2A and GOME-2B tropospheric NO<sub>2</sub>, SO<sub>2</sub> and HCHO products using MAX-DOAS observations from 2011 to 2014 in Wuxi, China: investigation of the effects of priori profiles and aerosols on the satellite products, *Atmos. Chem. Phys.*, 17, 5007–5033, <https://doi.org/10.5194/acp-17-5007-2017>, 2017.
- 25 Wang, Y., Apituley, A., Bais, A., Beirle, S., Benavent, N., Bruchkouski, A.B. I., Chan, K.L., Donner, S., Drosoglou, T., Finkenzeller, H., Friedrich, M.M., Friess, U., Garcia-Nieto, D., Gómez-Martín, L., Hendrick, F., Hilboll, A., Jin J.L., Johnston, P., Koenig, T. K., Kreher, K., Kumar, V., Kyuberis, A., Lampel, J., Liu, C., Liu, H.R., Ma, J.Z., Polyansky, O.L., Postlyakov, I., Querel, R., Saiz-Lopez, A., Schmitt, S., Tian, X., Tirpitz, J.L., Van Roozendael, M., Volkamer, R., Wang, Z.R., Xie, P.H., 30 Xing, C.Z., Xu, J., Yela, M., Zhang, C.X., Wagner, T.: Inter-comparison of MAX-DOAS measurements of tropospheric HONO slant column densities and vertical profiles during the CINDI-2 Campaign, submitted to *Atmos. Meas. Tech.*, 2019.
- 35 Wang, Y.S., Yao, L., Wang, L.L., Liu, Z.R., Ji, D.S., Tang, G.Q., Zhang, J.K., Sun, Y., Hu, B., Xin, J.Y.: Mechanism for the formation of the January 2013 heavy haze pollution episode over central and eastern China[J], *SCIENCE CHINA: Earth Sciences*, 57(1), 14-25. doi: 10.1007/s11430-013-4773-4, 2014.
- 40 Wittrock, F., Oetjen, H., Richter, A., Fietkau, S., Medeke, T., Rozanov, A., and Burrows, J. P.: MAX-DOAS measurements of atmospheric trace gases in Ny-Ålesund – Radiative transfer studies and their application, *Atmos. Chem. Phys.*, 4, 955–966, doi:10.5194/acp-4-955-2004, 2004.
- Yilmaz, S.: Retrieval of Atmospheric Aerosol and Trace Gas Vertical Profiles using Multi-Axis Differential Optical Absorption Spectroscopy, PhD thesis, University of Heidelberg, 2012.



- Zhang, Y.L., Cao, F.: Fine particulate matter (PM<sub>2.5</sub>) in China at a city level[J]. *Sci. Rep.*, 5, 14884, 2015.
- 5 Zielcke, J.: Observations of reactive bromine, iodine and chlorine species in the Arctic and Antarctic with Differential Optical Absorption Spectroscopy, PhD thesis, <https://doi.org/10.11588/heidok.00018932>, 2015.



**Table 1. Parameter settings used in the RTM. Default values are indicated by \*.**

Parameters	
Target species	aerosol, NO <sub>2</sub>
Wavelength (nm)	360, 477
Single scattering albedo (SSA)	0.8, 0.9*, 1.0
Asymmetry parameter (AP)	0.65, 0.72*
Solar zenith angle(SZA, °)	20, 40, 60, 80
Relative azimuth angle (RAA, °)	30, 60, 120, 180
Elevation angles (EA, °)	1, 2, 3, 4, 5, 6, 8, 15, 30, 90
Aerosol optical depth (AOD)	0.1, 0.3, 1.0, 3.0, 5.0
NO <sub>2</sub> Vertical column density (VCD, 10 <sup>16</sup> molec./cm <sup>2</sup> )	0.1, 0.3, 1.0, 3.0, 10.0
Profile types and parameters	Exponential: scale heights 0.2, 0.5*, 1.0* km
	Gaussian: peak heights 0.5, 1* km; peak widths 0.2, 0.5*, 1.0, 1.5 km
	Boltzmann: heights 1.0, 1.5*, 2.0 km

**Table 2. List of retrieval algorithms used in the comparison**

Algorithm	Forward Model	Method
PriAM	SCIATRAN version 2.2	OEM (Optimal Estimation Method)
MAPA	McArtim	Parameterized retrieval in combination with Monte Carlo approach

**Table 3. List of SSA and AP values used for the sensitivity studies (for the standard retrievals SSA = 0.9 and AP = 0.72 were used).**

Parameters	
SSA	0.7, 0.8, 1.0
AP	0.65, 0.68, 0.76, 0.80

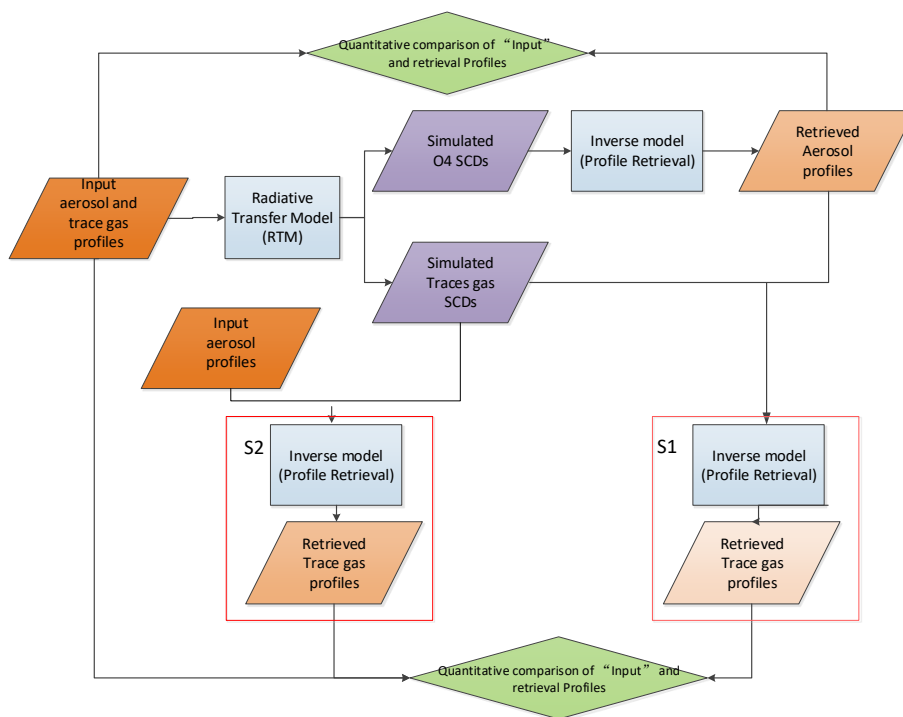


**Figure 1.** Flow diagram depicting the strategy used for the analysis of the effects of high aerosol loads on the retrieval of aerosol and trace gas profile

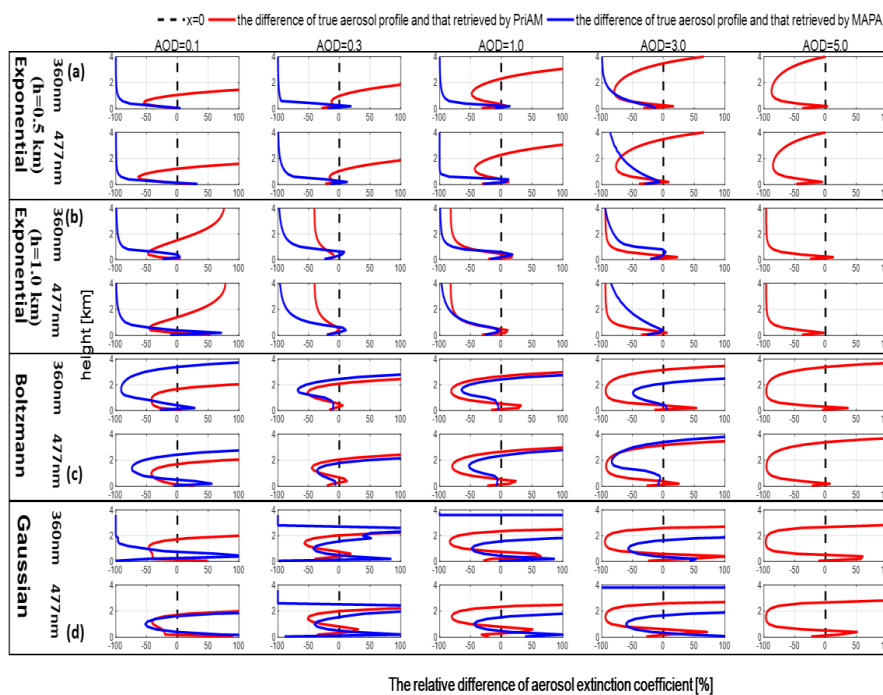


**Figure 2.** Relative deviations between the profiles retrieved by PriAM and MAPA for 360 nm (first line) and 477 nm (second line) and the corresponding input aerosol profiles for (a) exponential shape with  $h = 0.5$  km, (b) exponential shape with  $h = 1.0$  km, (c) Boltzmann shape, and (d) Gaussian shape.

The red and blue curves indicate the results from PriAM and MAPA, respectively. The direct comparison of the retrieved and input profiles is given in Fig. S8. The corresponding absolute deviations are shown in Fig. S9. Note that MAPA by default flags cases where the retrieved AOD exceeds 2, thus the high aerosol scenarios are missing for MAPA.

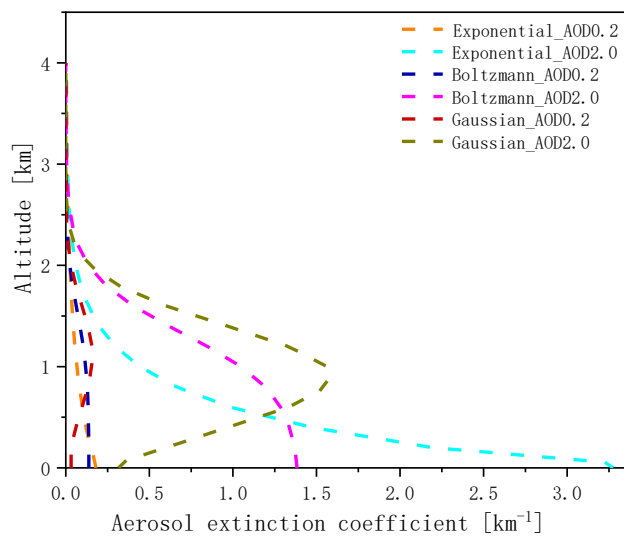
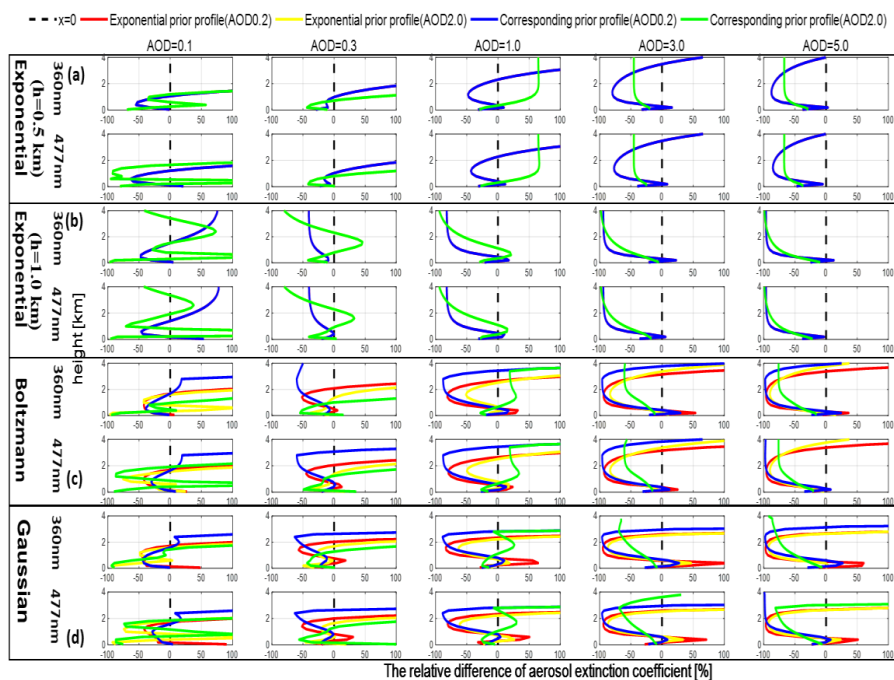


Figure 3. Different aerosol *a priori* profiles used by PriAM in this study.



**Figure 4.** Relative deviations of the PriAM aerosol inversion results with different alternative a priori profiles and the results for the universal a priori (exponential shape with AOD 0.2).

The first line in every panel denotes the results for 360 nm, and the second line denotes the results for 477 nm. Colors indicate the shapes and AODs shown at the top. ‘Corresponding a priori profile’ means that the same profile type as the simulated profiles is also used as a priori profile.



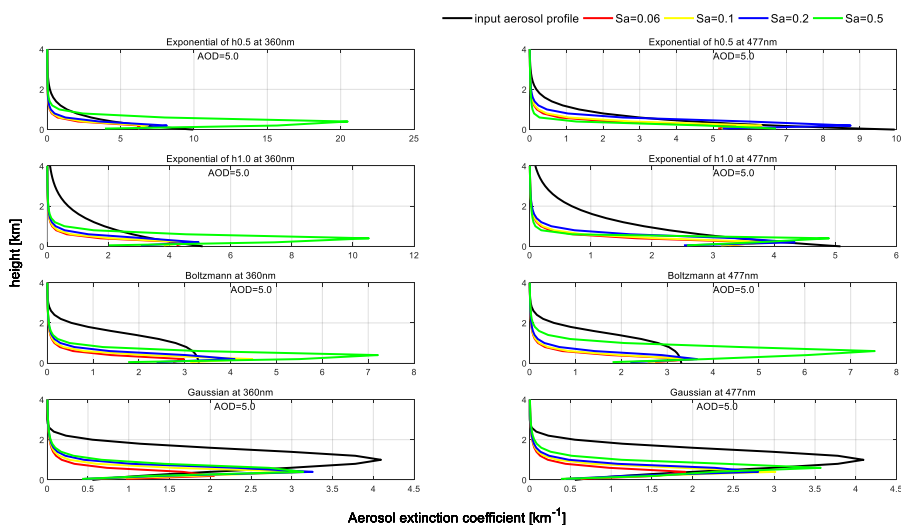


**Figure 5. Results for three aerosol profile shapes retrieved by PriAM for an AOD of 5.0 by using different values of the *a priori* profile covariance matrix (*S<sub>a</sub>*).**

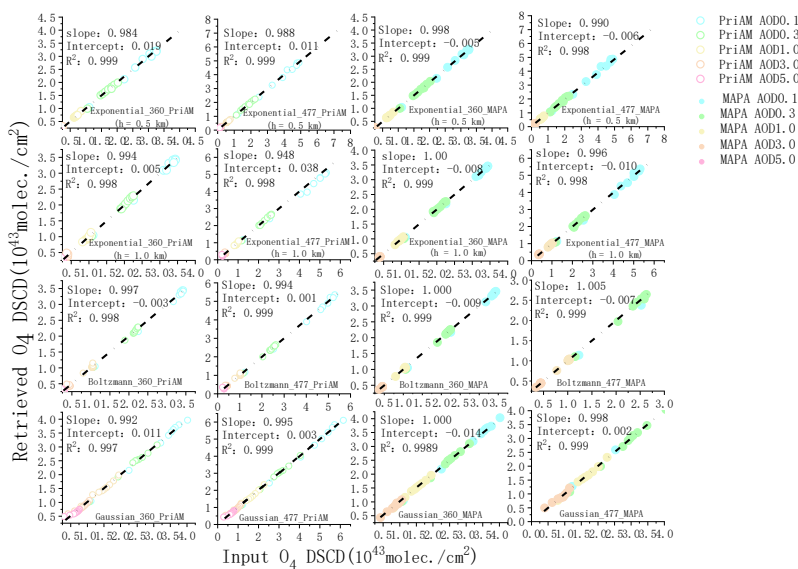


**Figure 6. Correlation plots between the retrieved  $O_4$  DSCDs and the input  $O_4$  DSCDs for PriAM and MAPA**

The open and closed circles denote the retrieved  $O_4$  DSCDs from PriAM and MAPA, respectively.

The colors refer to the AOD shown at the top right.

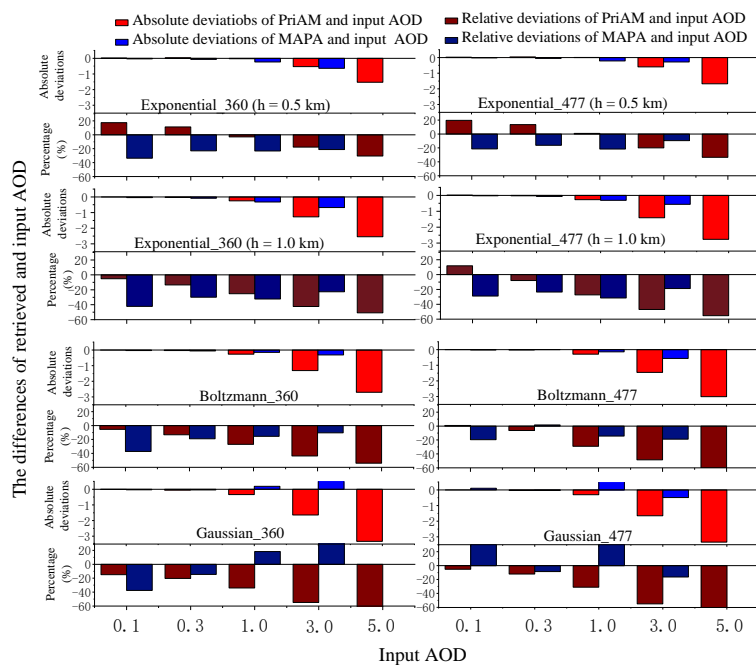


**Figure 7.** Comparison between the retrieved AODs and input AODs for PriAM and MAPA for the 4 aerosol profile shapes listed in table 1.

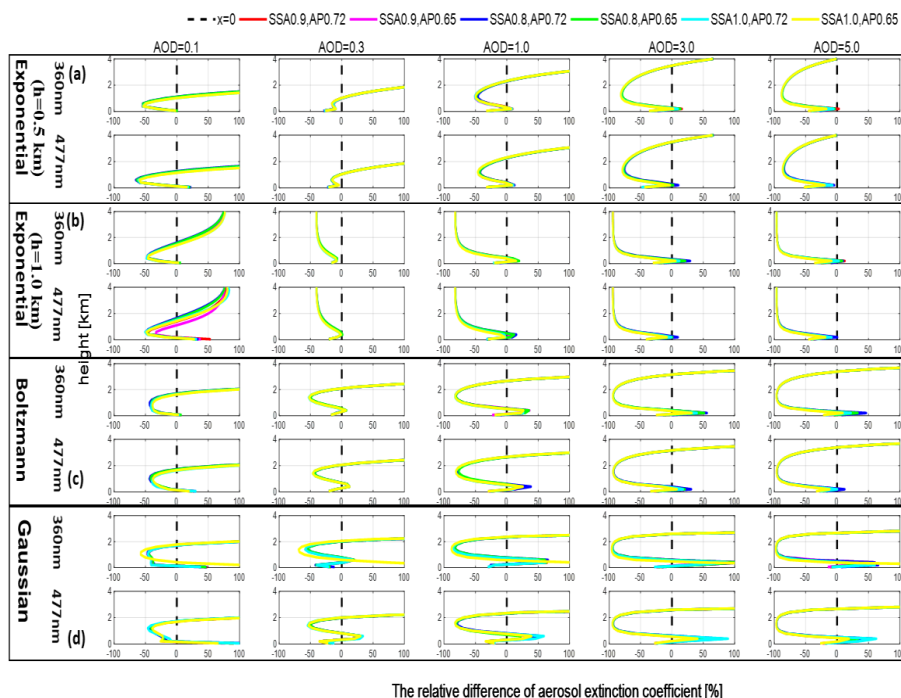


**Figure 8.** Relative deviations between the PriAM results using different SSA and AP and the input aerosol profile results for (a) exponential shape with  $h = 0.5$  km, (b) exponential shape with  $h = 1.0$  km, (c) Boltzmann shape, and (d) Gaussian shape. For these inversions, the same SSA and AP were used for the simulations of the  $O_4$  DSCDs and for the PriAM inversions. The first line in every panel denotes the results for 360 nm, and the second line denotes the results for 477 nm.

The colors refer to the corresponding SSA and AP values shown at the top.

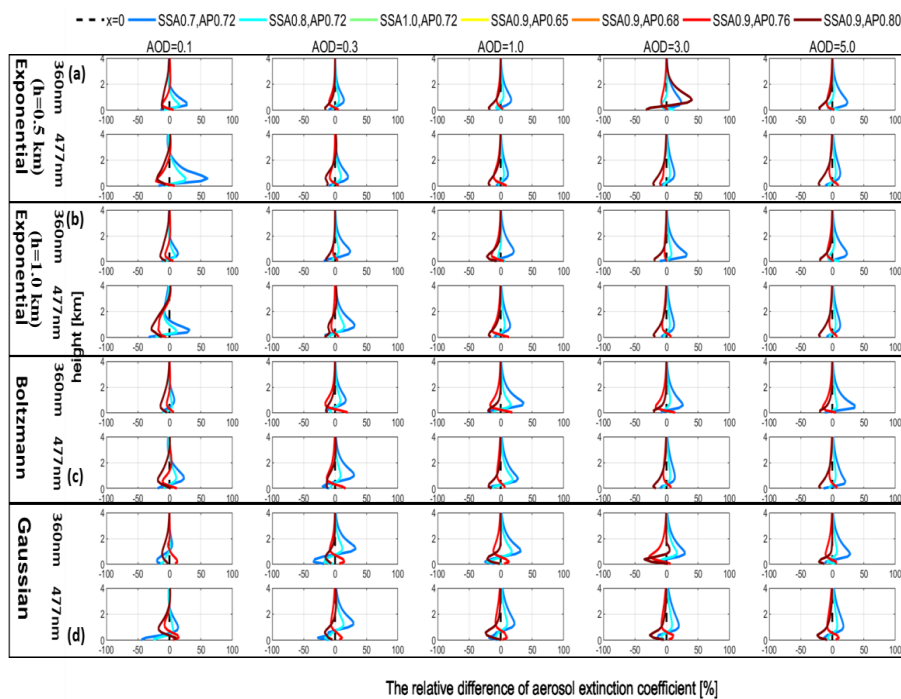


**Figure 9.** Relative deviations of the retrieved profiles using incorrect SSA and AP values from the retrieved profiles with the correct SSA and AP values for (a) exponential shape with  $h = 0.5$  km, (b) exponential shape with  $h = 1.0$  km, (c) Boltzmann shape, and (d) Gaussian shape

The colors refer to the SSA and AP values shown at the top.

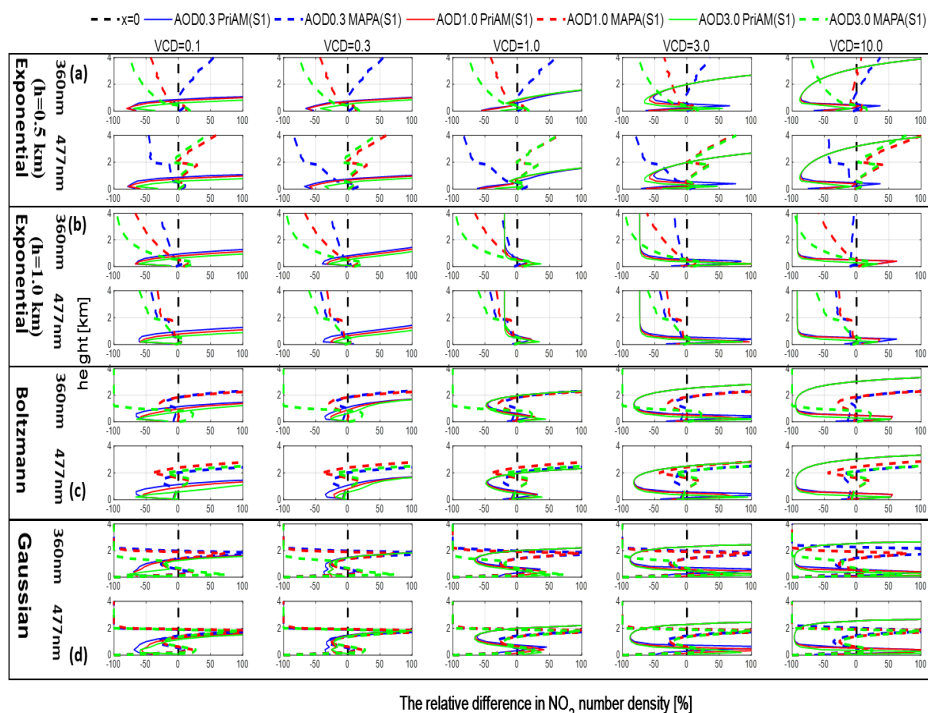


**Figure 10.** Relative deviations of the retrieved  $\text{NO}_2$  profiles by PriAM and MAPA from the input  $\text{NO}_2$  profiles for scenario S1 (see text) for aerosol profiles with 3 selected AODs (0.3, 1.0, and 3.0) and 5  $\text{NO}_2$  VCDs for of (a) exponential shape with  $h = 0.5$  km, (b) exponential shape with  $h = 1.0$  km, (c) Boltzmann shape, and (d) Gaussian shape.

The solid and dotted colored lines refer to the AODs and algorithms shown at the bottom right.

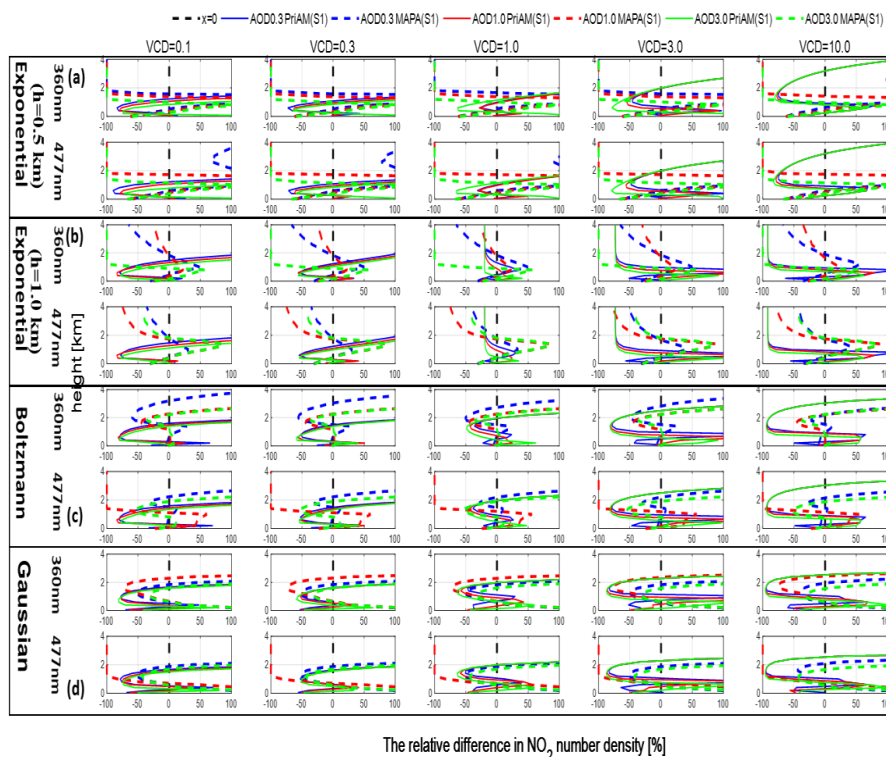


**Figure 11.** Relative deviations of the retrieved  $\text{NO}_2$  profiles for Boltzmann  $\text{NO}_2$  input profiles by PriAM and MAPA from the input  $\text{NO}_2$  profiles for scenario S1 (see text) and for 4 aerosol profile shapes ((a) exponential shape with  $h = 0.5$  km, (b) exponential shape with  $h = 1.0$  km, (c) Boltzmann shape, and (d) Gaussian shape) with 3 selected AODs (0.3, 1.0, and 3.0) and 5  $\text{NO}_2$  VCDs. The solid and dotted colored lines refer to the AODs and algorithms shown at the bottom right.

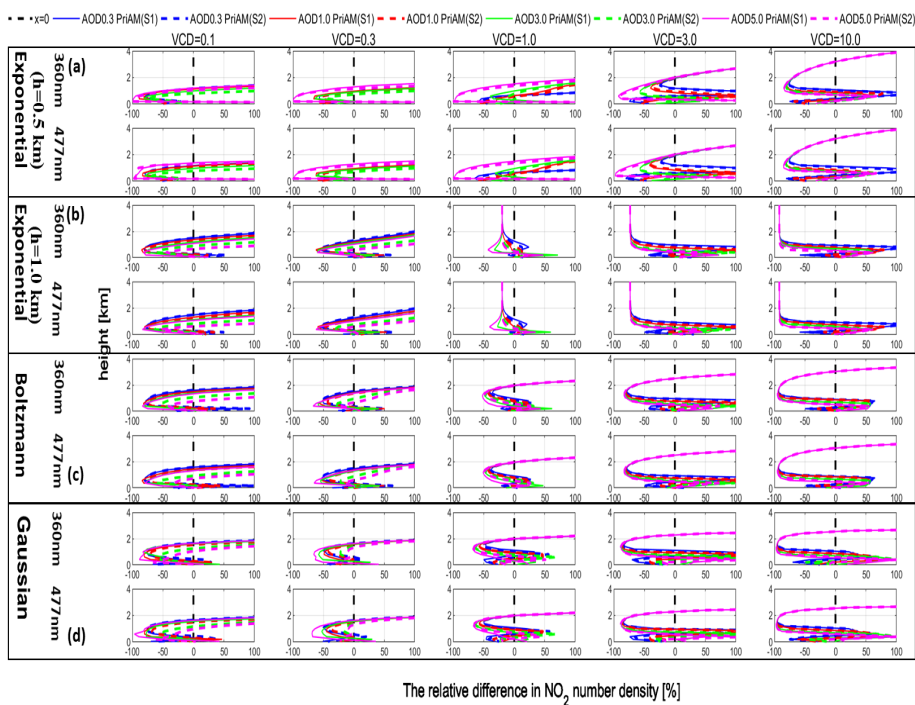


**Figure 12.** Relative deviations between the  $\text{NO}_2$  profiles retrieved by PriAM for scenarios S1 and S2 and the input  $\text{NO}_2$  profiles for 4 AODs (0.3, 1.0, 3.0, and 5.0) and 5 VCDs and for the (a) exponential shape with  $h = 0.5$  km, (b) exponential shape with  $h = 1.0$  km, (c) Boltzmann shape, and (d) Gaussian shape. The first line in each panel denotes the results for 360 nm, and the second line denotes the results for 477 nm.

The solid and dotted colored lines refer to the AODs and strategies shown at the bottom right.

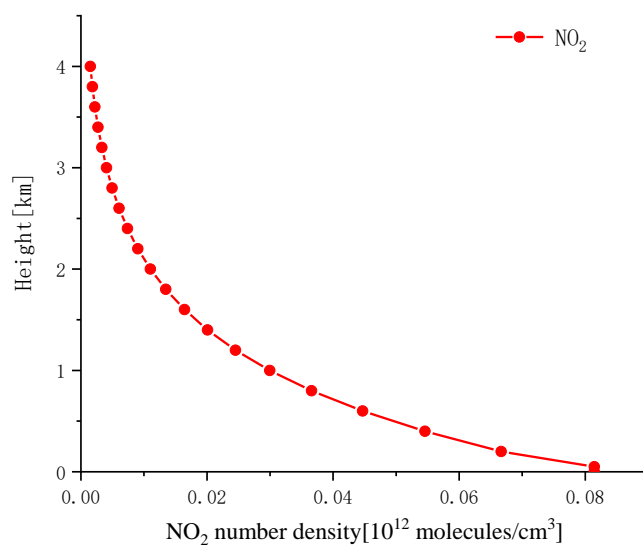
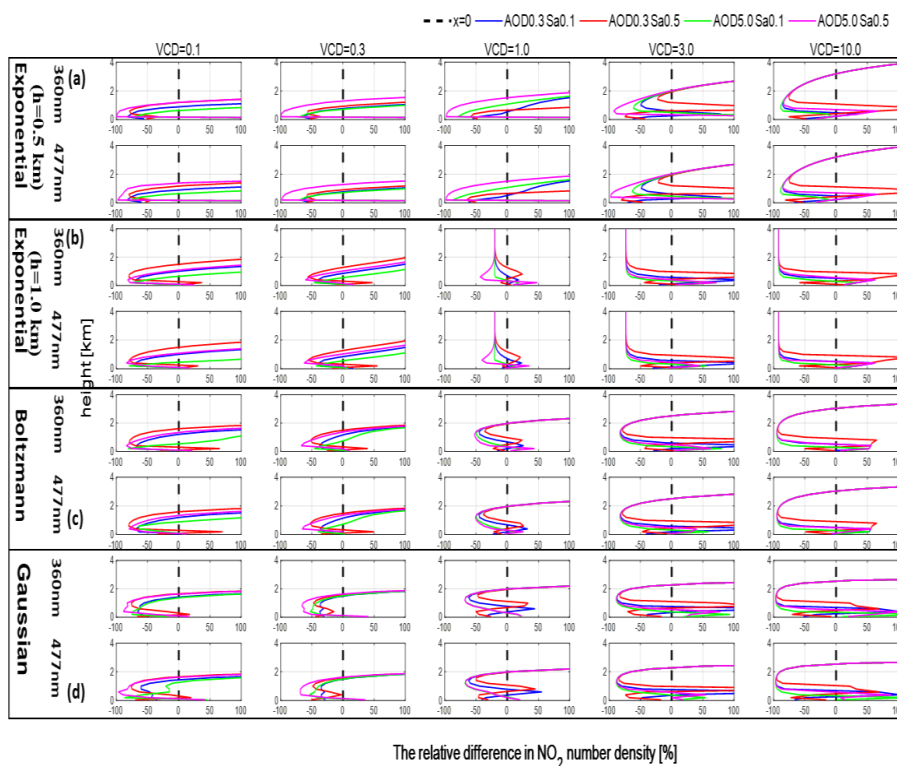


Figure 13. The *a priori* NO<sub>2</sub> profiles used by PriAM for NO<sub>2</sub> the retrieval in this study.





**Figure 14.** Relative deviations for  $\text{NO}_2$  profiles retrieved by PriAM and the input  $\text{NO}_2$  profiles for Sa of 0.1 and 0.5 and AOD of 0.3 and 5.0 and for (a) exponential shape with  $h = 0.5$  km, (b) exponential shape with  $h = 1.0$  km, (c) Boltzmann shape, and (d) Gaussian shape.

The first line in each panel denotes the results for 360 nm, and the second line denotes the results for 477 nm. The solid and dotted colored lines refer to the AODs and Sa shown at the top.

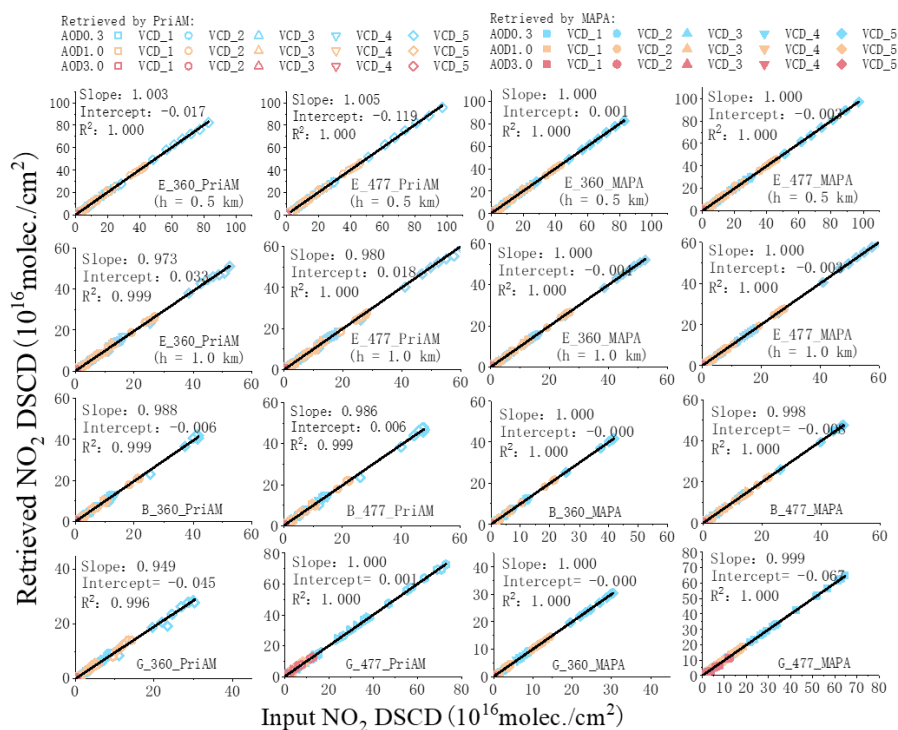


**Figure 15. Correlation plots between the retrieved NO<sub>2</sub> DSCDs by PriAM and MAPA versus the input NO<sub>2</sub> DSCDs for 3 AOD scenarios and 5 VCDs for scenario S1**

The colors refer to the VCD values and algorithms shown at the top.

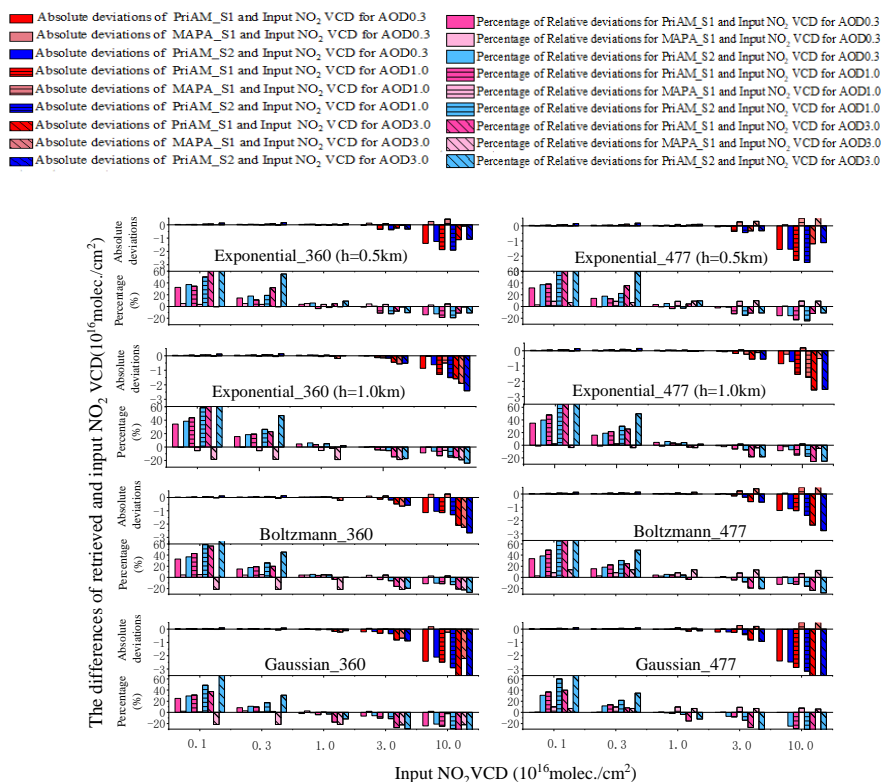


**Figure 16. Absolute and relative deviations between the retrieved and input NO<sub>2</sub> VCDs for PriAM (S1 and S2) and MAPA (S1) for 3 AOD scenarios and 5 VCDs.**

The colors and shapes refer to the deviations of the retrieved and input NO<sub>2</sub> VCDs of the different algorithms at different AODs shown at the top.